UNIVERSITAT ROVIRA I VIRGILI

DEEEA
Departament d'Enginyeria Electrònica, Elèctrica i Automàtica

GRADUATED STUDENT MEETING

on

ELECTRONIC ENGINEERING

Tarragona, June 19-20, 2008

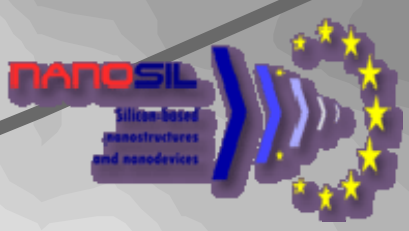

DIPUTACIÓ DE TARRAGONA

Abstracts Book

Graduated Student Meeting

on

Electronic Engineering

Tarragona, June 19-20, 2007

Organising Comitee

Xavier Vilanova

Lluis F. Marsal

Josep Ferré-Borrull

Margarita Rebenaque

Mireia Alberich

Marcos Alba

Programme

Schedule			
Thursday June 19th		**Friday June 20th**	
9:15	Opening Session		
9:30	Plenary session 1	9:30	Plenary session 4
	"Tungsten Oxide Nanorods: Synthesis, Application and Structural Investigation" **Dr. C. Blackman** *Department of Chemistry, University College London,* United Kingdom		**"Compac Model for Symmetric Double-Gate MOSFETS"** **Dr. A. Cerdeira** *CINVESTAV-IPN,* México
10:30	Cofee break	10:30	Cofee break
11:00	Plenary session 2	11:00	Plenary session 5
	"Basic Understanding of Dynamical Systems" **Dr. B. Robert** *Université de Reims,*France		**"Light propagation and light-matter interaction in Silicon photonic crystals"** **Dr. D. Gerace** *CNISM and Dipartimento di Fisica "Alessandro Volta," Università di Pavia,* Italy.
12:00	Plenary session 3	12:00	Plenary session 6
	"Current Injection Methods in Three Phase Rectifiers" **Dr. P. Pejović** *University of Belgrade,* Serbia		**"Selected Characterization Techniques for SOI Materials and Devices"** **Dr. S. Cristoloveanu** *IMEP - INP Grenoble MINATEC* France
13:00	Lunch	13:00	Lunch
14:30	Poster session 1	14:30	Poster session 1
15:30		15:30	Closing session and best poster awards

Invited Speakers

Plenary sesion 1

"Tungsten Oxide Nanorods: Synthesis, Application and Structural Investigation"

Dr. C. Blackman

Department of Chemistry, University College London, United Kingdom

Plenary sesion 2

"Basic Understanding of Dynamical Systems"

Dr. B. Robert

Université de Reims, France

Plenary sesion 3

"Current Injection Methods in Three Phase Rectifiers"

Dr. P. Pejović

University of Belgrade, Serbia

Plenary sesion 4

“Compac Model for Symmetric Double-Gate MOSFETS”

Dr. A. Cerdeira

CINVESTAV-IPN, México

Plenary sesion 5

"Light propagation and light-matter interaction in Silicon photonic crystals"

Dr. D. Gerace

CNISM and Dipartimento di Fisica “Alessandro Volta,” Università di Pavia, Italy.

Plenary sesion 6

"Selected Characterization Techniques for SOI Materials and Devices"

Dr. S. Cristoloveanu

IMEP - INP Grenoble MINATEC, France

Index

Invited Speakers

Posters

Plenary Sessions

“Tungsten oxide nanorods: Synthesis, application and structural investigation”

C. Blackman

Thin films of monoclinic WO_3 and WO_{3_x} have been synthesised by atmospheric pressure chemical vapour deposition from WCl_6 and three oxygen containing precursors; water, ethanol and ethanoic anhydride. A wide variation in the colour, crystal morphology and preferred orientation of the films was observed, depending on the chosen oxygen source. Gas-sensors were fabricated and the crystal morphology found to have a dramatic effect on the viability of the sensor.

Séminaire Bruno ROBERT

Résumé :
La conférence traite des systèmes dynamiques et de leurs solutions. Différents types de systèmes dynamiques sont définis en temps continu et en temps discret. Leurs propriétés sont présentées. Une attention particulière est portée aux systèmes dissipatifs et à leurs comportements. Après avoir introduit quelques concepts théoriques concernant les attracteurs, les solutions asymptotiques des systèmes dynamiques en temps continu sont présentées. Chaque notion nouvelle est illustrée d'exemples pratiques.

Abstract:
The conference deals with dynamical systems and their solutions. Different kinds of dynamic systems are defined in continuous time and discrete time. Their properties are presented. Particular attention is paid to dissipative systems and their behaviors. After having introduced some theoretical concepts about attractors, asymptotical solutions of dynamical continuous time systems are presented. Each new concept is illustrated with practical examples.

Bibliographic summary

Dr. Bruno ROBERT received the M.Sc in electrical engineering and power electronic from the Ecole Normale Superieure of Cachan and University of Paris VI, in 1988, and Ph.D. degrees in computer science, automation and signal processing from the University of Reims, in 1993. He ranked first at the Agregation in electrical engineering in 1987. Agrégation is the highest national competitive examination for teaching positions in undergraduate schools and universities in France. Since 1993, he is an assistant professor at the University of Reims and it work as a research director.
He is 15 years experienced in the field of power electronic and electric drives. Since 1997, he investigates nonlinear dynamics of electric drives and power stages by applying chaos theory. His main research areas are transient modes of quasi-resonant converters, bifurcation analysis and chaos control in current inverters and time series analysis and control of step motors, linear motors and fuel cell systems. These studies include modeling, simulation and control aspects and experimental investigations.
Dr. Bruno ROBERT is co-author of more than 40 journal and conference papers and serves as reviewer for many international journals. He is a member of the CReSTIC Laboratory at the University of Reims-Champagne-Ardenne.

Current Injection Methods In Three-Phase Rectifiers

Predrag Pejović

Current injection as a method to reduce THD of the input currents in three-phase rectifiers. Current injection methods: third harmonic, square-wave, and the optimal. Methods to provide current injection, current injection devices and current injection switching networks. Current injection methods in diode bridge rectifiers, third harmonic and the optimal. A historical glimpse: “people just write papers, no one bothers to read.” Power taken by the resistance emulator and the efficiency issues. Resistance emulators. Current-loaded and voltage-loaded resistance emulators. Active and passive resistance emulators. Resistance emulators in square-wave current injection, current-injection-based twelve-pulse rectifiers. New results: application of the current injection methods in twelve-pulse autotransformer-based rectifiers; twelve-pulse rectifier requiring eight diodes.

Predrag Pejović was born in Belgrade, Yugoslavia, in 1966. He received the B.S. and M.S. degrees in electrical engineering from the University of Belgrade, in 1990 and 1992, respectively, and the Ph.D. degree from the University of Colorado, Boulder, in 1995. In 1995, he rejoined the University of Belgrade, where he is presently Professor and Head of the Department of Electronics. His current research interests are in dynamics of nonlinear systems, analog circuit design, three-phase high power factor rectifiers, electronic measurements, techniques for computer-aided analysis and design of power electronic systems, and spatial positioning algorithms.

COMPACT MODEL FOR SYMMETRIC DOPED DOUBLE-GATE MOSFETS

Antonio Cerdeira Altuzarra

Double-Gate (DG) transistors are considered a very attractive option of the Silicon-On-Insulator (SOI) MOSFETs to improve the performance of CMOS SOI devices. Some advantages are: reduced short channel effects; lower parasitic capacitances; increased circuit speed; stronger control of the channel by the gate; reduced drain-induced barrier lowering, threshold voltage roll-off and off-state leakage. DG transistors are very attractive for applications in low power and low voltage digital and analog integrated circuits.

The demand of an accurate and CAD compatible compact model for DG MOSFETs is a really urgent task, reason why many researchers are dealing with it. The main problem for modeling fully depleted DG devices is that the potential at the surface and the potential at the middle of the silicon layer are related and can not be treated independently one from the other. In addition, the electric field and gate voltage of the device as function of these potentials are expressed by transcendental equations that do not have analytical solution.

In this talk we present a new compact analytical model for symmetric double-gate MOSFETs transistors that for the first time considers the doping concentration of the silicon layer variable from undoped to $3x10^{18}$ cm^{-3}. First, the core model for long channel devices is presented, which was later complemented in order to include the followings short channel effects: VT variation with channel length reduction and DIBL; velocity saturation effects; series resistance; channel shortening and subthreshold slope degradation. The model for short channel devices requires only six parameters to extract. Validation using 2D simulation for both high and low doped devices, is presented. Finally, modeled and experimental measurements of FinFETs working in the temperature range from 20 °C to 200 °C are compared.

Light propagation and light-matter interaction in Silicon photonic crystals

Dario Gerace, Lucio Claudio Andreani
CNISM and Dipartimento di Fisica "Alessandro Volta," Università di Pavia, Italy

Silicon photonics is emerging from the era of speculative research and slowly moving its first steps into market applications. The main motivations rely on the forthcoming need for fast optical interfaces between microelectronic circuitry and communication technology, which in perspective should be low-cost and CMOS-compatible to be implemented for mass production. In order to *siliconize* photonics, there are two main areas or building blocks for investigation: (*i*) generating the light, and (*ii*) selectively guiding and transporting it within Silicon.

A possibile route towards these two goals is given by the use of photonic crystal integrated circuits made on Silicon platforms, i.e. nanostructured Si-based wafers in which the periodicity of the refractive index is exploited to tailor the on-chip light confinement and propagation.

In this talk we will give an overview of our recent research lines with Silicon-based photonic crystals, mainly related to the two points quoted above. Specific topics that will be discussed are: efficient light generation and extraction in 2D Silicon-based photonic crystal slabs, and the role of disorder and fabrication imperfections in the photonic crystal pattern on the propagation losses in line-defect waveguides.

[1] D. Gerace and L.C. Andreani, Optics Letters **29**, 1897 (2004).
[2] D. Gerace and L.C. Andreani, Optics Express **13**, 4939 (2005).
[3] D. Gerace and L.C. Andreani, Photonics and Nanostructures **3**, 120 (2005).
[4] D. Gerace *et al*., Applied Physics Letters **87**, 211116 (2005).
[5] M. Galli *et al*., Applied Physics Letters **88**, 251114 (2006).
[6] L.C. Andreani and D. Gerace, Physica Status Solidi B **244**, 3528 (2007).

Selected Characterization Techniques for SOI Materials and Devices

Sorin Cristoloveanu
IMEP, INPG - Minatec, BP 257, 38016 Grenoble, France (sorin@enserg.fr)

SOI is a necessary technology, with multiple facets that need to be correctly captured and understood. The goal of this tutorial is to offer a comprehensive view of the general strategy and dedicated methods for electrical characterization. It is not aimed to provide an exhaustive catalogue of techniques, instead it is designed to be practical and provide helpful guiding for conducting proper measurements.

The evaluation of SOI structures is hampered by several problems: thinness of the film, presence of the BOX, stacked interfaces, typical defects, strain, etc. The electrical properties are of uppermost interest as they directly impact on the design and performance of integrated circuits. A number of conventional methods can be borrowed from bulk Si and adapted to SOI whereas other methods are no longer applicable in thin films. Fortunately novel techniques, such as the pseudo-MOS transistor (Ψ- MOSFET), can be conceived and implemented. The ingredients of the Ψ -MOSFET will be described, based on examples demonstrating why it became a successful and efficient routine technique for SOI material evaluation at the wafer level. Several alternatives (Hg-FET, Hall effect, etc) will be addressed.

We will next see how to manipulate single-gate and multiple-gate MOSFETs in order to reveal, from their static and dynamic characteristics, key parameters like carrier mobility and lifetime, threshold voltage, self-heating, leakage currents, etc. Various parameter extraction methods for the evaluation of the series resistance, interface traps and oxide defects will be explicited and critically compared. A direct application is the monitoring of radiation-induced damage and hot-carrier reliability effects. More sophisticated techniques like split-CV, geometric magnetoresistance and lowtemperature transport are very successful for universal mobility characterization in very advanced MOSFETs. The charge pumping, transient currents, and noise spectroscopy will also be evoked.

We will see the appropriate treatment for multiple channels. Independently, each channel informs on the quality of the nearby interface. The multi-channel coupling effects are more complex and basically have a two-fold impact: they alter the measurement signature but, in turn, they can be taken advantage of for detailed analysis of the physics mechanisms.

BIOGRAPHY : SORIN CRISTOLOVEANU

Sorin Cristoloveanu received the PhD (1976) in Electronics and the French Doctorat ès-Sciences in physics (1981) from the National Polytechnic Institute, Grenoble (INPG), France. He joined the Centre National de la Recherche Scientifique (CNRS) and became a Senior Scientist in 1982 and a Director of Research in 1989. In 1989, he joined the University of Maryland, College Park, as an Associate Professor for one sabbatical year. He also worked at JPL (Pasadena), Motorola (Phoenix), and the Universities of Florida (Gainesville), Nashville and Western Australia (Perth). From 1993 to 1999, he served as the director of the LPCS Laboratory of INPG. Between 1999—2000, he was in charge of the creation of the Center for Advanced Projects in Microelectronics (CPMA Grenoble), initial seed of the Minatec center. He is the author or co-author of more than 600 technical journal papers and communications at international conferences (including 100 invited contributions). He is the author or the editor of 17 books, and he has organized 16 international conferences. His expertise is in the area of the electrical characterization and modeling of semiconductor materials and devices, with special interest for silicon-on-insulator structures. He has supervised more than 60 PhD completions. With his students, he has received 5 Best Paper Awards, an Academy of Science Award (1995), and the Electronics Division Award of the Electrochemical Society (2002). He is a Fellow of IEEE, a Fellow of the Electrochemical Society, and Editor of Solid-State Electronics.

Posters

ELECTRO-THERMAL SIMULATION OF PRECONCENTRATION MEMBRANES USING FINITE ELEMENTS TOOLS.

Roser Inglés[1*], Jordi Pallarés[2], Jose Luis Ramírez[1],
Xavier Vilanova[1], Xavier Correig[1], Eduard Llobet[1]
[1]MINOS, Dept. of Electronic, Electrical and Automatic Control Engineering, ETSE, Universitat Rovira i Virgili, Tarragona, Spain
[2]Department of Mechanical Engineering School of Chemical Engineering Universitat Rovira i Virgili, Tarragona, Spain
[*] roser.ingles@urv.cat 977.25.65.72

Abstract

We use finite element simulation in order to study the electro-thermal behaviour and optimise the membrane design for a preconcentrator. We run dynamic simulations in order to obtain the system time response. We run stationary simulations in order to study the temperature distribution. To enhance discrimination capabilities, an active area temperature homogeneity in steady state better than 15 K is needed. We will develop heater designs and introduce a silicon plug in order to reach this specification.

1. Introduction

Preconcentration is necessary in order to sense traces of toxic gases that are in air in a very low concentrations. A preconcentrator is used to adsorb these traces of toxic gases during a period of time. Then the full amount of adsorbed gas is released, by means of a temperature step in the absorbent material, thus obtaining an increased concentration. [1-3]

Membranes in literature were developed for sensors, so they are smaller than membranes for preconcentrators and their objective is minimize power consumption[4-6]. We will use a preconcentration membrane so our application is different and our objectives also. We are aimed to design membranes implemented in silicon having large area, good temperature homogeneity and small thermal inertia.

We use finite element simulation in order to study the electro-thermal behaviour and optimise the membrane design.

2. Initial design

Our first design was developed in the Centre Nacional de Microelectrònica (CNM) in Barcelona. It's a membrane of 3000 μm x 1000 μm with an active area of 2500 μm x 500 μm. It's composed by a silicon substrate chemically etched, a dielectric sandwich membrane SiO2/Si3N4/SiO2 to ensure the thermal insulation of the structure and a platinum heater with double spiral shape. The layers of the dielectric membranes are fabricated as follows: thermal oxidation at 1100 ºC in order to grow 1000 Å of a SiO2 layer, a LPCVD deposition of 3000 Å of Si3N4 layer and a PECVD deposition of 8000 Å of SiO2. The platinum heater has a thickness of 2500 Å. The heater is designed to have a separation of 50 μm and its width 50 μm in the side sticks, 80 μm in the central stick and 120 μm in the electrical contacts. A titanium layer is deposited prior to Pt to promote the heater adhesion to the substrate.

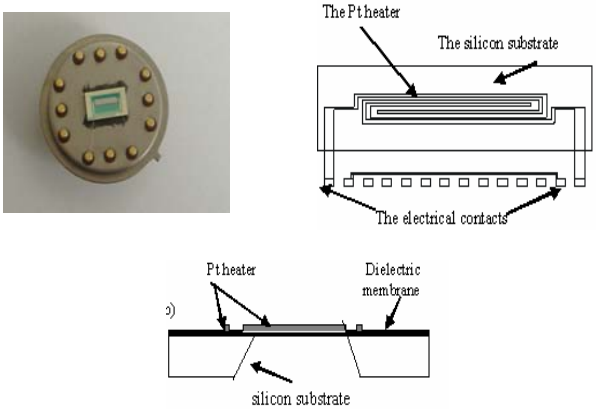

Fig. 1. a) A view from the top of the membrane **b)** A cross sectional view of the membrane

We run dynamic simulations in order to obtain the system time response. Raising time was in the order of tens milliseconds, so it's acceptable to be used in systems with sensors with a time response of tens of seconds.

To enhance discrimination capabilities if they are in the membrane specification set, an active area temperature homogeneity in steady state better than 15 K is needed.

Evaluating the 3D temperature distribution in our device, for a 500 K steady peak temperature, the maximum temperature difference was more than 100 Kelvin degree, so we need to modify heater design in order to improve this results.

Stationary Simulations :

Maximum temperature:	500 K ± 2 K
Power consumption:	76.88 mW
Difference temperature:	> 150 K

Dynamic Simulations :

Rising time:	≈50 ms

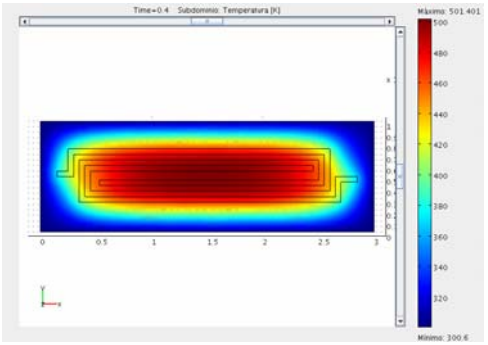

Fig. 2. Simulation of the initial design

3. Heater design

We design different heaters shapes and we improve this results to 60 Kelvin degree.

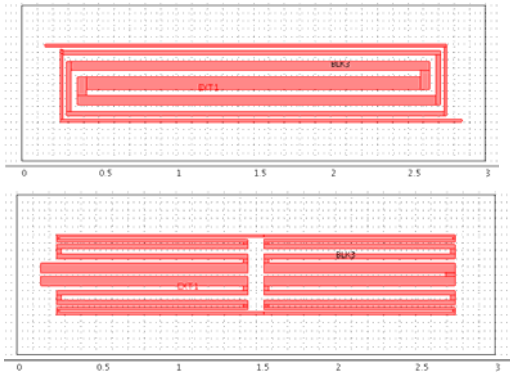

Fig. 3. Some heater design

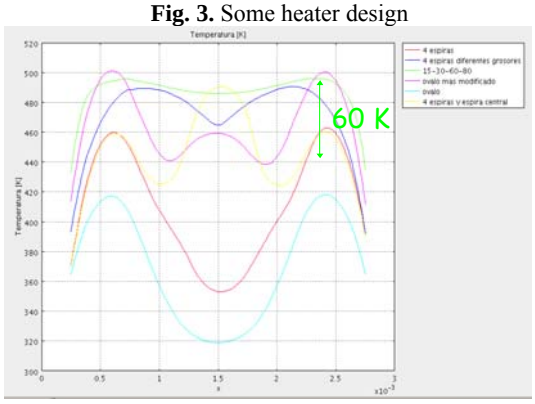

Fig. 4. Heater design results

4. Silicon plug

A greater improvement in temperature homogeneity is reached using a silicon plug under the membrane.[7] With this we are able to homogenise to a maximum difference of about fifteen Kelvin degrees, depending on the thickness of the silicon plug.

A study of power consumption as a function of distance from silicon plug to the membrane edge has been developed.

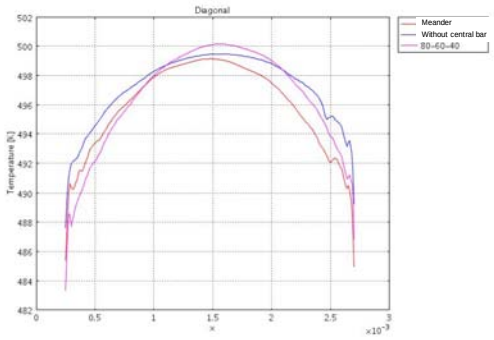

Fig. 5. Simulation results using a silicon plug

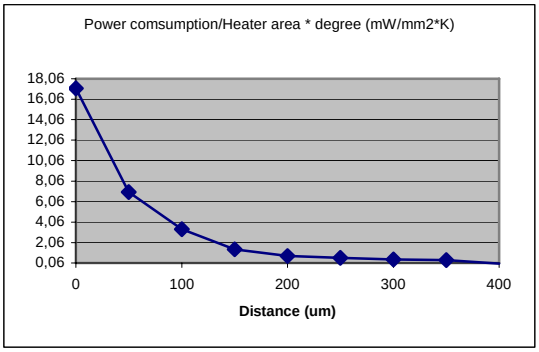

Fig. 6. Study of power consumption as a function of distance from silicon plug to the membrane edge

5. Further work

We will introduce the mechanical behaviour in order to avoid the breakdown of membrane reaching the highest dimensions. Then we will simulate the fluid dynamics.

Acknowledgment

This work is financially supported by the CICYT project (TEC2006-03671)

References

1. Nakamoto, T., et al.," Odor-sensing system using preconcentrator with variable temperature". Sensors and actuators B-Chemical, 2000.
2. Manginell, R., et al. "Microfabricated planar preconcentrator." in Tech. Digest 2000 Sol.-State Sensor and Actuator Workshop. 2000. Cleveland.
3. Grate, J., et al.," Progressive thermal desorption of vapor mixtures from a preconcentrator with a porous metal foam internal architecture and variable thermal ramp rates". Analytical chemistry, 2005.
4. Lu, C., et al.," A dual-adsorbent preconcentrator for a portable indoor-VOC microsensor system". Analytical chemistry, 2001.
5. Swart, N., et al.," Design optimization of integrated microhotplates". Sensors and actuators A-Physical, 1994.
6. Belmonte, J., et al.," High-temperature low-power performing micromachined suspended micro-hotplate for gas sensing applications". Sensors and actuators B-Chemical, 2006.
7. Briand, D., et al.," Design and fabrication of high-temperature micro-hotplates for drop-coated gas sensors". Sensors and actuators B-Chemical, 2000.

Improvement of MS based E-nose performance by the incorporation of chromatographic retention time as a new data dimension

Cosmin Burian, Maria Vinaixa, Jesus Brezmes and Xavier Correig

Department of Electronic Engineering, Universitat Rovira i Virgili, Avenida Paisos Catalans 26, 43007 Tarragona, Spain

Abstract

This paper presents the work done in order to improve the performance of mass spectrometry-based electronic noses using the time retention of a chromatographic column as additional information (dimension). Solutions of nine isomers of dimethylphenols and ethylphenols were used in this experiment. The gas chromatograph mass spectrometer response was analyzed with Partial Least Squares (PLS), PLS-Discriminanat Analysis (PLS-DA) and multi-way PLS (n-PLS) algorithms, showing that the combined information gives better results.

1. Introduction

The goal of this work is to improve the sensitivity and/ or selectivity of an MS based Electronic Nose by using the combination of Gas Chromatography and Mass Spectrometry adding a third dimension to the dataset representing the time parameter of the chromatographic separation. To optimize the analysis, different chromatographic retention times were investigated.

Even though in recent experiments the MS electronic nose has proven better than gas sensor based multisensor systems, some complex mixtures have proved difficult to classify. In most of the cases the methods used for the classifications were two-way methods. By coupling a gas chromatograph to a mass spectrometer we have the possibility to extract more data adding the time dimension to the m/z fractions and their intensity.

2. Materials and methods

For the experiment design we looked at 2 aspects: the PCA of the 9 isomers mass spectra and their chromatographic retention time. To obtain the chromatographic retention time (Fig.1.), 9 solutions of 1% isomer in methanol containing only one isomer were prepared and analyzed. In order to see which of the 9 isomers has most alike mass spectra we performed a PCA of the theoretical mass spectra of each isomer (Fig.2.).

Based on this information we designed the experiment as shown in **Table 1.** Benzene acts as an internal standard, and having the highest concentration it is used in the normalization pretreatment of the data. The experiment was designed in order to having a challenging sample set for the mass spectra-based electronic nose.

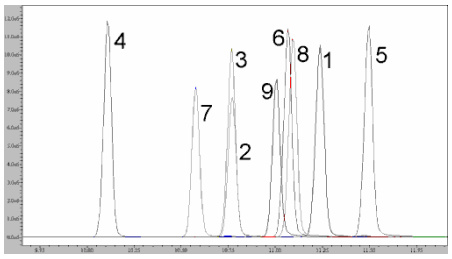

Fig.1. Chromatographic retention times for the 9 isomers as follows: **1)** 2,3-Dimethylphenol;**2)** 2,4-Dimethylphenol;**3)** 2,5-Dimethylphenol;**4)** 2,6-Dimethylphenol;**5)** 3,4-Dimethylphenol;**6)** 3,5-Dimethylphenol;**7)** 2-Ethylphenol;
8) 3-Ethylphenol and **9)** 4-Ethylphenol;

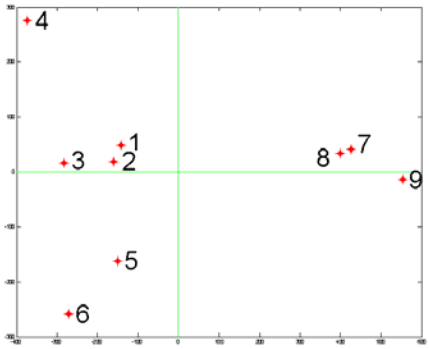

Fig.2. Principal Component Analysis of the isomers mass spectra

Three chromatographic methods were used. In method one, we tried to separate as much as possible the isomers. To achieve this, a temperature programmed separation was used, starting at 50°C, where the temperature was kept constant for one minute, until 180°C, where almost all the isomers were separated. Method two and three were designed to give more coeluted peaks, and therefore isothermal separations. The temperatures used were used 175°C and 190°C respectively. The measurements were conducted through syringe injection of 1 µl per measurement, and ten repetitions for each method and solution were made. Two blanks were also measured, one consisting of just methanol and the other with methanol and 2% of benzene.

component	Sol1	Sol2	Sol3	Sol4	Sol5	Sol6	Sol7	Sol8	Sol9	Sol10	Sol11	Sol12	Sol13	Sol14	Sol15	Sol16	Sol17	Sol18	Sol19	Sol20
2,3-Dimethylphenol	-	0.5	0.5	0.5	0.5	0.5	0.5	0.5	0.5	0.25	0.5	0.5	0.5	0.5	0.5	0.5	0.25	0.5	0.25	0.5
2,4-Dimethylphenol	0.5	-	0.5	0.5	0.5	0.5	0.5	0.5	0.5	0.5	0.25	0.5	0.5	0.5	0.5	0.5	0.5	0.25	0.5	0.25
2,5-Dimethylphenol	0.5	0.5	-	0.5	0.5	0.5	0.5	0.5	0.5	0.5	0.5	0.25	0.5	0.5	0.5	0.5	0.5	0.5	0.5	0.5
2,6-Dimethylphenol	0.5	0.5	0.5	-	0.5	0.5	0.5	0.5	0.5	0.5	0.5	0.5	0.5	0.5	0.5	0.5	0.5	0.5	0.5	0.5
3,4-Dimethylphenol	0.5	0.5	0.5	0.5	-	0.5	0.5	0.5	0.5	0.5	0.5	0.5	0.5	0.5	0.5	0.5	0.5	0.5	0.5	0.5
3,5-Dimethylphenol	0.5	0.5	0.5	0.5	0.5	-	0.5	0.5	0.5	0.5	0.5	0.5	0.25	0.5	0.5	0.5	0.5	0.5	0.5	0.5
2-Ethylphenol	0.5	0.5	0.5	0.5	0.5	0.5	-	0.5	0.5	0.5	0.5	0.5	0.5	0.25	0.5	0.5	0.25	0.25	0.5	0.5
3-Ethylphenol	0.5	0.5	0.5	0.5	0.5	0.5	0.5	-	0.5	0.5	0.5	0.5	0.5	0.5	0.25	0.5	0.5	0.5	0.25	0.25
4-Ethylphenol	0.5	0.5	0.5	0.5	0.5	0.5	0.5	0.5	-	0.5	0.5	0.5	0.5	0.5	0.5	0.25	0.5	0.5	0.5	0.5
B/Et-OH/acetone	2%	2%	2%	2%	2%	2%	2%	2%	2%	2%	2%	2%	2%	2%	2%	2%	2%	2%	2%	2%

Table1. Experiment design (the numbers represent percentage of substance into methanol)

3. Results and Discussion

The data collected from the GC-MS was arranged into a 3-D matrix (I x J x K) with the following directions: retention time (K), m/z ratio (J), and samples measured (I).

First, the data was pretreated for peak alignment, normalized and mean centered. The peaks were aligned in the three dimensional matrix using the RAFFT algorithm. After this first step data was separated into three datasets, the original untouched 3-D data, and by summing the m/z axis and time axis, we obtained the total ion chromatogram and the average mass spectra respectively.

All the three groups were normalized by the maximum value. The data was finally single-slab mean centered following the sample direction of the data in order to subtract the mean sample vector, leaving each sample containing just the relative differences.

Two more data groups were created, one by concatenating the average mass spectra with the total ion chromatogram, and a second one by unfolding the 3-D matrix.

This 5 groups of data can be separated into two main types, 2-D and 3-D data types. The 2-D data was analyzed by Partial Least Squares (PLS) and Partial Least Squares Discriminanat Analysis (PLS-DA), while the 3-D data was analyzed by multi-way PLS (n-PLS) and multi-way PLS-DA. In order to do this each dataset was separated into training and testing sets by a chosen training/test ratio of 7/3. The training set was used to train the PLS and n-PLS models. Onto these models the test set was projected.

The model and prediction performance were evaluated by means of the Root Mean Square Error of Cross-Validation (RMSECV), and the Root Mean Square Error of Prediction (RMSEP), respectively.

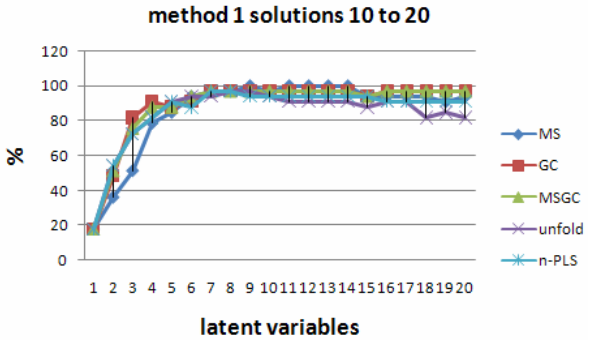

Fig.3.a. Prediction success tare for method 1

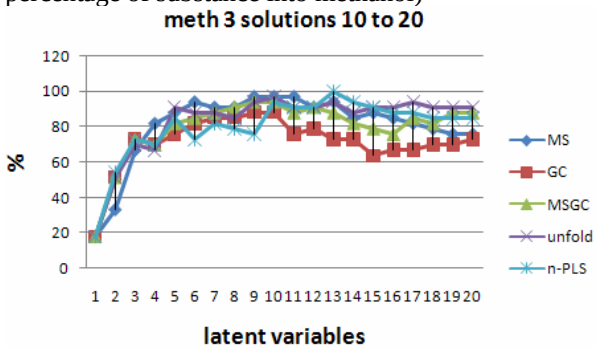

Fig.3.b. Prediction success tare for method 3

The data was proven difficult to classify and predict if all the 20 different mixtures were analyzed. Because of this, the first 9 solution were analyzed at first, followed by solutions 10 to 20.The overall prediction performance was a sample prediction success rate.

The results present the sample prediction success rate for methods one and three for solutions 10 to 20, and are shown in Fig.3. a and b.

We notice that method 3, in which the peaks are the most coeluted gives worse results than method 1, where a temperature programmed separation was employed in order to achieve a better separation. We can clearly notice this in the chromatographic data sample success rate.

Another interesting observation is that even though the average mass spectra seems to give a good performance classifying the samples, the combination of this information with the total ion chromatogram by means of unfolding or unifying the MS data with the TIC data almost always gives better results than MS or TIC data alone. Between the unfolded data and the unified MSGC data the later one is appearing to give better results and presents the advantage of an easier model interpretation.

The multi-way PLS model seems to present consistent results on both methods, yielding a high prediction success rate in both methods. It is also recommended over the unfolded and unified data because it builds a simpler and more parsimonious model. The n-PLS algorithm presented the best results in the most difficult case, the third method, solutions 10 to 20, giving 100% success rate classification for 13 latent variables.

4. Future Work

As a future work some new multi-way algorithms should be applied to this data. Also the combination of 2D algorithms (PCA, PLS and PLS-DA), and 3-D algorithms (PARAFAC, Tucker3 and-PLS) should be combined with fuzzy neural networks to evaluate them as data reduction algorithms.

Microdrop system applied to polymeric absorbent layer deposition for gas micropreconcentrators

D. Shaposhnik, X. Vilanova

DEEEA, Universitat Rovira iVirgili, Tarragona, Spain
Tel. +34 977 256 571, Fax +34 977 559 605 e-mail: dmitry.shaposhnik@urv.cat

Abstract

The microdrop system is sheduled to be used for polymeric absorbent deposition on micromachined membranes of a gas preconcentrator. Preparation of solutions suitable for the system and deposition of model substances were studied.

Introduction

A preconcentrator consists of an absorbent material placed on a heating support. The gas mixture to be analyzed flows through it and is accumulated during certain time into the absorbent. Then the mixture is desorbed by a temperature pulse and driven to the sensor array. The thermally released compounds provide narrow desorption peaks with relatively high concentration. It increases the sensitivity of the analysis with the gas sensors. Selectivity of analysis can be also increased by preconcentrator [1 – 3].

Conventional preconcentrators, or so called microtraps, consist of a stainless-steel or glass capillary tube packed with one or more granular adsorbent material [4 – 7]. Capillary tubes suffer from large dead volume and limited heating efficiency due to their larger thermal mass. Micromachining technology can overcome these limitations by significantly reducing the dead volume and thermal mass. Microheaters fabricated on dielectric membranes with low thermal mass have been reported for chemical sensing and other applications [8 – 12]. Similar structures coated with thin adsorbent films are used for preconcentration and focusing in the Sandia microsystem [13]. Up to date studies have shown that the fabrication of such devices with silicon technology offers a lot of advantages. The miniaturization leads to improvements of heating rates and power consumption.

The aim of our work is to design a micropreconcentrator that will increase sesor array sensitivity to volatile organic compounds. It is scheduled to produce the device by the means of microfabrication technology. A polymeric absorbent placed on microfabricated membrane will be used to decrease the thickness of absorbent layer and the power consumption of the preconcentrator. The method that will be used for absorbent deposition is ink jet printing.

Experimental

Ink jet system consists of a piezo-electrically driven microdispenser (A010-300), a camera with stroboscope unit for visual control of the operation, temperature controller, programmable control device *multi-dos* as computer interface, and software package (from GeSiM mbH).

The first task of the work is to find an absorbent which would satisfy the conditions essential for preconcentration. At first, sorbent should be sufficiently temperature stable (up to 200°C). Next, it should be possible to deposit it with ink jet printing, i.e. polymer must have viscosity low enough at deposition conditions and high enough one after annealing. Finally, polymer should have sufficiently high concentration factor.

It was decided to start with commercially available gas chromatography stationary phases of OV series. These absorbents are polymethyl-phenil polymers, as usual dissolved in silicon oil. OV-17 was used as absorbing layer in a micropreconcentrator in the work by Mitra and Kim [14].

Toset-up the ink jet printing method, glycerol was chosen as the most handy viscous substance. Ink jet printer has got a maximum allowed ink viscosity of 5 mPa·s. The value of glycerol viscosity was determined at various temperature with vibro viscosimeter SV-10 (A&D Company, Ltd).

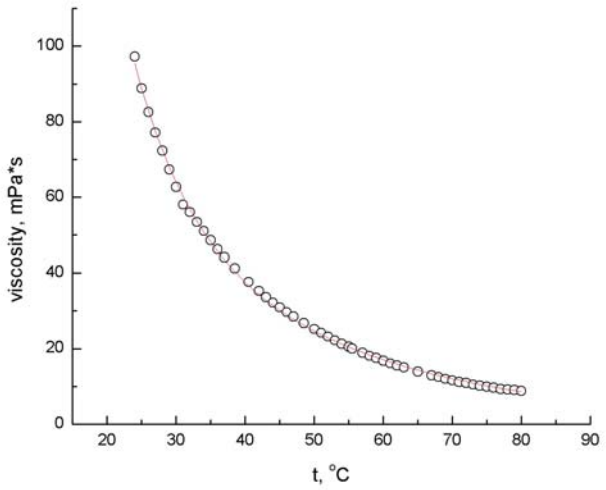

Fig. 1. Temperature dependence of glycerol solution viscosity, approximated with second order exponential decay

Temperature dependence for viscosity of 85% by volume glycerol in water solution was approximated with second order exponential decay (Fig. 1).

The glycerol solution was deposited on a glass object-plate. Deposition was carried out at 70°C, with frequency of 100 drops per second.

Results and conclusions

A 3×3 mm square of a glass object-plate was covered with the glycerol solution (Fig. 2).

Fig. 2. Glycerol solution deposited on a glass object-plate inside the 3×3 mm drawn square.

The obtained results show the possibility of the microdrop system use for the micromembrane covering with polimeric absorbents. However, deposition process must be more precise for this application.

The next step will include precise positioning of substrates and depositing polymeric absorbents on macrodimentioned silicon and alumina carriers.

References

[1] P. Ivanov, F. Blanco, I. Gràcia, N. Sabaté, A. Ruiz, X. Vilanova, X. Correig, L. Fonseca, E. Figueras, J. Santander, C. Cané. *Improvement of the gas sensor response via silicon μ-preconcentrator*. Sensors and Actuators B 127 (2007) 288–294

[2] B.A. Eckenrode, *The application of an integrated multifunctional fieldportable GC/MS system*, Field Anal. Chem. Tech. 2 (1998) 3–20.

[3] C.-J. Lu, J. Whiting, R.D. Sacks, E.T. Zellers, *Portable GC with tuneable retention and microsensor array detection for the determination of complex vapor mixtures*, Anal. Chem. 75 (2003) 1400–1409.

[4] W. Tian, S. Pang, C. Lu, E.T. Zellers, *Microfabricated preconcentrator-focuser for a micro scale gas chromatograph,* J. Microelectromech. Syst. 12 (2003) 264–272.

[5] S. Mitra and C. Yun, *Continuous gas chromatographic monitoring of low concentration sample streams using an on-line microtrap,* J. Chromatogr. A, vol. 648, pp. 415–421, 1993.

[6] C. Feng and S. Mitra, *Two-stage microtrap as an injection device for continuous on-line gas chromatographic monitoring,* J. Chromatogr. A, vol. 805, pp. 169–176, 1998.

[7] C.-Y. Peng and S. Batterman, *Performance evaluation of a sorbent tube sampling method using short path thermal desorption for volatile organic compounds,* J. Environ. Monit., vol. 2, pp. 313–324, 2000.

[8] C.-J. Lu and E. T. Zellers, *A dual-adsorbent preconcentrator for a portable indoor-VOC microsensor system,* Anal. Chem., vol. 73, pp. 3449–3457, 2001.

[9] N. Najafi, K. D. Wise, and J. W. Schwank, *A micromachined ultra-thin-film gas detector,* IEEE Trans. Electron Dev., vol. 41, pp. 1770–1777, 1994.

[10] G. Sberveglieri,W. Hellmich, and G. Müller, *Silicon hotplates for metal oxide gas sensor elements,* Microsyst. Technol., vol. 3, pp. 183–190, 1997.

[11] H. Baltes, O. Brand, and O. Paul, *CMOSMEMSTechnology and CAD: the case of thermal microtransducers,* in Proc. SPIE, vol. 3328, 1998, pp. 2–12.

[12] T. A. Kunt, T. J. McAvoy, R. E. Cavicchi, and S. Semancik, *Optimization of temperature programmed sensing for gas identification using micro-hotplate sensors,* Sens. Actuators, Chem. B., vol. 53, pp. 24–43, 1998.

[13] P. D. Moor, A. Witvrouw, V. Simons, and I. D. Wolf, *"The fabrication and reliability testing of Ti/TiN heaters,* in Proc. SPIE, vol. 3874, 1999, pp. 284–293.

[14] Minhee Kim, Somenath Mitra J. *A microfabricated microconcentrator for sensors and gas chromatography,* Chrom. A, 996 (2003) 1–11

Conduction mechanisms and photovoltaic properties of -crystalline-silicon /P3HT heterojunction Solar Cells

J.C. Nolasco[a], J. Pallares[a], L.F. Marsal[a], R. Cabre[a], M. Estrada[b], Y. Matsumoto[b]

jairocesar.nolasco@estudiants.urv.cat **T:977558524, F:977559605**
[a]Department d´Enginyeria Electrònica, Universidad Rovira I Virgili, Ave. Paisos Catalans, Tarragona, Spain
[b]Departamento de Ingeniería Eléctrica, Centro de Investigación y de Estudios Avanzados del IPN, Av. IPN 2508 Zacatenco, Mexico City 07360

Abstract

The conduction mechanism and photovoltaic properties of Au/ P3HT (poly [3-hexylthiophene])/n-type crystalline silicon (n-c-Si)/Al heterojuntion solar cells are presented. A P3HT layer was spin-coated on silicon substrate followed by thermal annealing and metal deposition. . The mechanisms of conduction over temperature range from 300K to 360K is Multi-step tunneling capture emission (MTCE) at low-medium voltages. Afterwards, the current-voltage characteristic is affected by a series resistance and SCLC (Space charge limited currents). The solar cell characteristics reported Voc=0.47 V and Isc=5.52 mA/cm^2. The conversion efficiency of the structure was 1.29 %.

Keywords: Hybrid photovoltaic cell, organic semiconductors, polythiophene

1. Introduction

Solar cells based on inorganic crystalline semiconductors as Si show high conversion efficiencies, up to 25%, and long term stability, but they suffer from the drawbacks of expensive processing, limited substrate area and stiffness. Another alternative was found in amorphous and microcrystalline semiconductors as a-Si:H, which meet the requirements of lower cost and larger substrate area, although their conversion efficiency is around 10%. Looking for other low cost alternatives, different structures and organic materials for solar cells have been studied [1,2]. These organic materials which can be processed at temperatures below 150 ^{o}C, and show light weight.

Organic materials can be divided into two classes regarding the way in which they are processed to deposit the films. Whereas small molecular weight materials are usually deposited from the gas phase by sublimation or evaporation, conjugated polymers are usually processed by spin-on. A representative polymer is an alkylthiophene derivative which has been successfully applied to the fabrication of organic TFTs, showing the highest mobility values [3]. In addition, this material presents a high optical absorption coefficient in the visible spectra [4].

At present, solar cells fabricated with all organic-based semiconductors suffer from low conversion efficiency, mainly associated with low diffusion length of excitons, low charge collection and transport efficiencies, as well as high density of recombination centers and traps. Nevertheless their reported efficiency at present is around 6%.

Many organic thin-film materials have been developed and applied for opto-electronic device preparation; however, there are still several doubts in its optical, electrical, as well as their charge transport mechanisms. In this sense, the combination of well known inorganic material as is crystalline-silicon could elucidate some of the mentioned doubts. So, hybrid heterojuntion, may represent an interesting alternative also to enhance the cost/efficiency relation by achieving a better solar spectrum use combining the simple processability of polymers, which can be deposited on large areas, as wide optical-gap window-layer in the solar cells with the stable inorganic semiconducting materials.

2. Experimental Procedure

An organic-inorganic hybrid structure consisting of Au/P3HT/n-type crystalline silicon (n-c-Si)/ Al heterojunction was prepared. The ohmic back-contacts were realized by thermal evaporation of Al. P3HT was spin-coated at 5000 rpm on an n-type silicon wafer with a doping level of 6 x 10^{15} cm-3. The structure was annealed at 120 ^{o}C. The polymer film thickness was 80 nm, determined by ellipsometry and unintentionally doping determined by CV curves was between 6.9x10^{16} cm-3-8.8x10^{16} cm-3. Gold top contacts 30 nm thick were deposited by sputtering, using a mechanical mask.

3. Results and Discusions

The expected energy diagram of the heterojunction is shown in figure 1. It was built using properties of the layers reported in the literature [4].

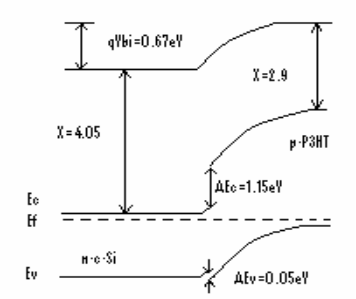

Figure 1. An energy diagram of the n-c-Si/p-P3HT

In order to analyze this device, an equivalent circuit model was used. It is show in figure 2.

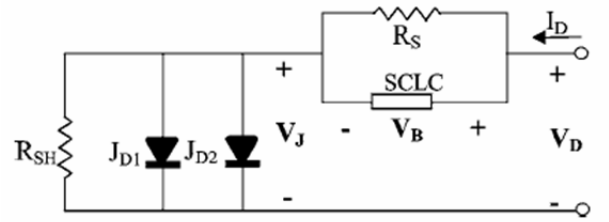

Figure 2. Electrical equivalent circuit

We adjust the experimental measurements with one diode.

$$J_D = Jo \exp[A \cdot V] \qquad (1)$$

where

$$Jo = B \exp(\frac{-Ea}{kT})$$

The figure 3 show the temperature depende of A and Jo.

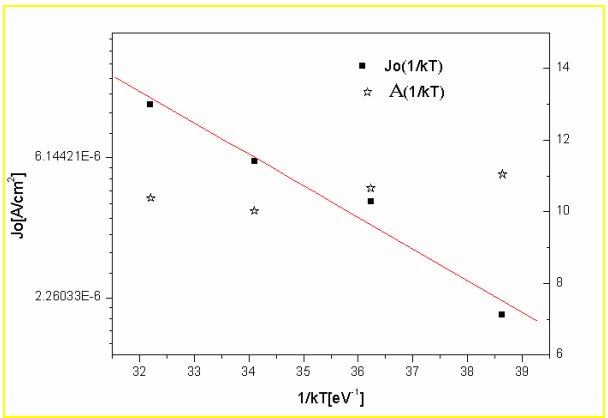

Figure 3. Temperature dependence of Jo and A

The A parameter in the last figure is almost constant, which is a characteristics of tunneling mechanism. Also Jo has activation energy of 225meV that correspond at Fermi level of the Silicon. It mean that a Multi-step tunneling capture emission mechanism is present in this device.

The diode area was 0.031 cm^2. The I-V characteristic at AM1.5 illumination resulted in Voc=0.47 V, Isc=5.52 mA/cm^2, FF=0.37, and a conversion efficiency of 1.29 %.

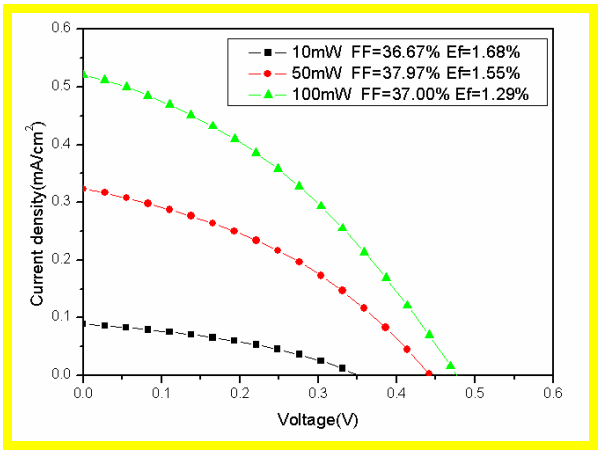

Figure 4. Photocurrent-voltage characteristics

4. Conclusions

The mechanisms of conduction over temperature range from 300K to 360K is Multi-step tunneling capture emission (MTCE) at low-medium voltages. Afterwards, the current-voltage characteristic is affected by a series resistance and SCLC. The solar cell characteristics reported Voc=0.47 V and Isc=5.52 mA/cm^2. The conversion efficiency of the structure was 1.29 %.

References

1. H. Hoppe and N.S. Sariciftci, J. Mater.Res., 19, 1924 (2004).
2. J-M Nunzi, C.R. Physique, 3, 523 (2002).
3. H. Sirringhaus, N. Tessler, R. H. Friend, Synth. Met, 102, 857 (1999).
4. M. Onoda, and K. Tada, Proceedings of International Symposium Electrical Insulating Material, Himeji, Japan, p.595 (2001).
5. L.F. Marsal, P. Pallares, X. Correig, A. Orpella, D. Bardes and R. Alcubilla, J. Appl. Phys., 85, 1216 (1999).

Deposition and characterization of tungsten oxide layers by Aerosol Assisted Chemical Vapour Deposition (AACVD) for metal oxide gas sensors

T. Stoycheva[1*], X. Correig[1],

[1] DEEEA, Universitat Rovira iVirgili , Spain
[*]Toni Stoycheva, Departament d'Enginyeria Electrònica, Electrica i Automàtica, URV
Avinguda dels paisos Catalans, 26 Campus Sescelades, 43007 TARRAGONA (Spain)
Tel. +34 977 256 571, e-mail: toni.stoycheva@urv.cat

Abstract

Every year more and more developments and novelties are strongly needed in the area of gas sensors in order to improve the quality of life in our society. The sensing properties of gas sensors are strongly depend on the sensing materials and the deposition methods used. In this paper we will deal with the deposition of tungsten trioxide layers by Aerosol Assisted Chemical Vapor Deposition (AACVD). This method is very flexible and allows the deposition of different metal oxides used for gas sensors. Moreover, the AACVD method provides also facility to work under atmospheric or low pressure conditions. These are the main goals that our group takes into account for starting this investigation. In this paper, an AACVD system will be designed and used to deposit tungsten oxide layer for gas sensors.

1. Introduction

The already known methods used for the deposition techniques of metal oxides for gas sensors could be divided in three main groups: a) Paste/slurry deposition, including Screen-printing and Drop coating, b) CVD techniques and c) Physical Vapor Deposition (PVD), which include Evaporation, Sputtering and Ion plating; this are standard process mostly used in semiconductor industry. The main difference between layers deposited by screen-printed or drop coating and CVD or PVD is related with it's thickness and porosity, which can influence the sensing properties of the gas sensors. In [1], Prof. Perkin's group have studied the deposition, analysis and functional properties of tungsten oxide films deposited by AACVD. In another work they present the properties of deposited tungsten oxide layers in more detail and focused on the effect of film thickness [2].

This paper describes our preliminary work in this area. The new challenges of our group, based on this AACVD deposition system will be:

1. deposition over the structural or porous substrate;
2. design and fabrication of masks for depositing different materials for sensor arrays;
3. limited deposition by heating only active area of the gas sensor;
4. next implementation and adaptation to gas sensors

Our group designed an AACVD system. The whole system, which is described in this paper, was set-up and first deposition tests were made over glass substrates.

2. Design and fabrication

The AACVD reactor was home-designed and fabricated by stainless steel in our technical services. Two heater cartridges with a thermocouple have been embedded into it. Temperature of it can be controlled up to 600 ºC. The deposition system has also the possibility to operate under either vertical(A) or horizontal(B) flux directions. The cross-section of the reactor it`s shown in Fig.1

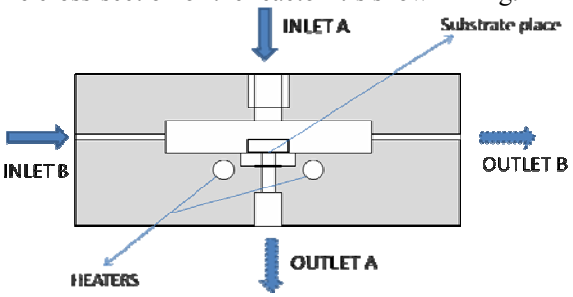

Fig.1 Cross-section of the AACVD reactor

The AACVD reactor was then implemented and connected to the whole deposition system. The deposition system includes: AACVD reactor; ultrasonic bath; temperature controller; flux meter and tube connections. After set-up the system, we made first deposition tests. In Fig. 2 you can observe a schematic related with an AACVD process. A single source precursor is dissolved in an organic solvent (1) and is converted into droplets by an ultrasonic modulator (2). The aerosol of precursor and solvent is then transported by a carrier gas into a hot zone where it evaporates. The vapour of the precursor is then transported to the substrate where it absorbs and reacts to form a film and by-products (3) and (4).

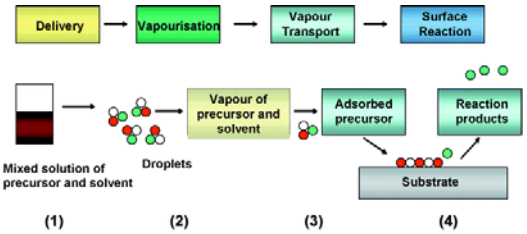

Fig.2 Schematic representation of the AACVD process

3. Experimental part

3.1. Equipment and experimental details

AACVD experiments were conducted using the horizontal bed reactor described before. The tungsten trioxide layers deposition have been made over sheets of glass substrates. The glass was cleaned prior to be used by washing with acetone and dried in air. Then placed and heated in the chamber of the reactor. The temperature was monitored by a temperature controller. The precursor tungsten hexacarbonyl [$W(CO_6)$] was dissolved in toluene and placed into a bottle. An aerosol was generated at room temperature using a CHICCO ultrasonic humidifier. Nitrogen gas flowing at 500mL/min passes through the aerosol mist and forces the aerosol droplets into the reactor chamber. The reactor was heated to the required temperatures and then the nitrogen line was open to carry the aerosol into the reactor. The gas flow continued until all the precursor mixture is over. In our case, it was typically after 1 hour. The reactor was cooled to the room temperature and then opened. The whole experimental circuit is shown in Fig.3

Fig.3 Experimental AACVD system set-up

3.2. First deposition tests

The deposition tests were realized under different experimental conditions, taking into account several dependences on temperature, flux rate, concentration of the compounds, time of deposition, etc. The experimental parameters used are shown in table 1.

Table1. Experimental parameters of depositions

Temperature (ºC)	Deposition time (min)	Volume of Toluene(mL)	Weight of [$W(CO_6)$] (g)
500	60	30	0,15
500	60	25	0,11
500	150	25	0,13
400	60	10	0,05
500	60	10	0,05
600	60	10	0,05

3.3. Film analysis

Scanning electron microscopy (SEM and ESEM) were used for detailed analysis and observation of the deposited layers. We obtain two typical tungsten oxide layers, a) randomly orientated needles (fig.3a) at 600ºC and b) compact grain layers (fig.3b) at 400ºC. In Fig.4, spectral analysis confirms the presence of tungsten in the deposited layers. The thickness will be measured in our coming work.

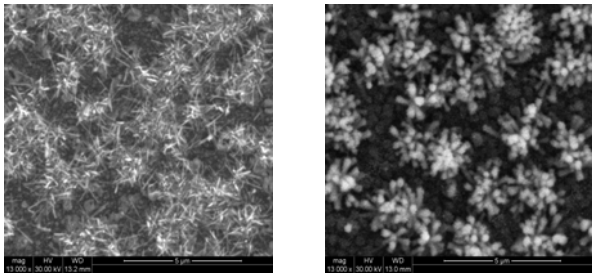

(a) **(b)**

Fig.3 SEM picture of [$W(CO_6)$] obtained (a) at 600ºC (b) at 400ºC.

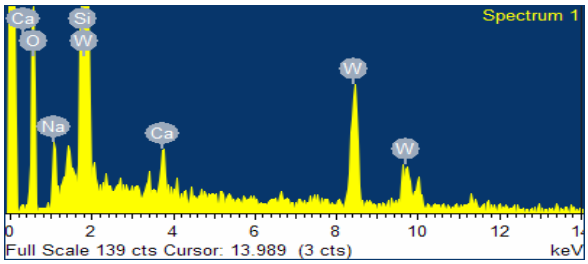

Fig.4 The spectral analysis show presence of tungsten

7. Summary and conclusion

An AACVD system has been successfully designed and seted-up. It works under atmospheric pressure, which provides facility of preparation and implementation of the processes needed for the deposition of metal oxides for gas sensors. We have been able to deposit successfully tungsten oxide layers over glass substrates, using tungsten hexacarbonyl as a precursor.

References

[1] **S. Ashraf, C. S. Blackman, R. G. Palgrave, S. C. Naisbitt, and I. P. Parkin, "Aerosol assisted chemical vapour deposition of WO3 thin films from tungsten hexacarbonyl and their gas sensing properties," *Journal of Materials Chemistry*, vol. 17, pp. 3708-3713, 2007.**

[2] **S. Ashraf, C. S. Blackman, S. C. Naisbitt, and I. P. Parkin, "The gas-sensing properties of WO3-x thin films deposited via the atmospheric pressure chemical vapour deposition (APCVD) of WCl6 with ethanol," *Measurement Science & Technology*, vol. 19, 2008.**

Estimación de parámetros para la máquina de inducción, a partir de datos de catálogo y aspectos constructivos, con algoritmos de fácil implementación

Jaramillo Matta, Adolfo Andrés; Guasch Pesquer, Luis.
Grupo de Automática y Electrónica Industrial
Departamento de Ingeniería Eléctrica, Electrónica y Automática
Universidad Rovira i Virgili, Tarragona, España
email: adolfoandres.jaramillo@urv.cat, luis.guasch@urv.cat, Tel: 977 556 579, 977 559 675

Abstract

En este trabajo se diseña un algoritmo de estimación de parámetros para el modelo de jaula sencilla de la máquina de inducción trifásica, basado en la minimización del error producido entre puntos reales de funcionamiento y aproximaciones de comportamiento de la máquina de inducción, generadas por el mismo algoritmo. Esta técnica ajusta mejor los parámetros, respecto a otras técnicas analizadas en este trabajo. El algoritmo utiliza los datos de catálogo, placa característica y aspectos constructivos de la máquina para la estimación de sus parámetros. También se realiza un análisis de error entre los resultados de este algoritmo y otras técnicas utilizadas para el mismo fin.

1. Introducción

La estimación de parámetros de un modelo es un proceso determinante para el correcto modelado del comportamiento de un sistema. En el caso de la máquina de inducción trifásica existen diferentes modelos, entre ellos: jaula sencilla y doble jaula, como se muestra en la Figura 1. Una vez escogido el modelo, se conoce la cantidad y naturaleza de los parámetros a estimar y se determina si se consideran constantes o variables. El siguiente paso consiste en recopilar los datos necesarios para realizar la estimación, por ejemplo: datos de catálogo, placa de características, ensayos, etc. Por último es necesario aplicar un algoritmo de cálculo que permita la obtención de los parámetros.

Tanto en la adopción del modelo como en la selección de los datos necesarios para realizar la estimación existen pocas variaciones en la bibliografía especializada. Sin embargo, sorprende la enorme variación de propuestas respecto a los algoritmos de cálculo, no observándose hasta el momento una tendencia de referencia. En este trabajo se presenta un nuevo algoritmo de fácil implementación con una técnica de estimación paramétrica basada en aproximaciones de comportamiento, partiendo de los datos de catálogo y de aspectos constructivos de la máquina a modelar. También se realiza un estudio de tres tipos de error, entre el algoritmo desarrollado y otras técnicas utilizadas para estimar estos parámetros.

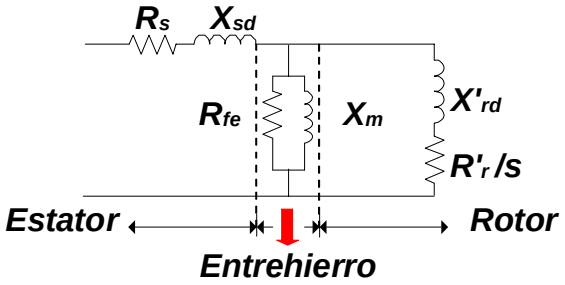

Fig.1. Modelo por fase de la máquina de inducción trifásica de jaula sencilla

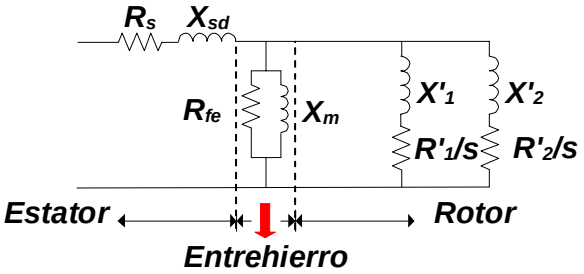

Fig.2. Modelo por fase de la máquina de inducción trifásica de doble jaula

2. Modelo de la máquina de inducción

Las máquinas de inducción trifásicas pueden estar constituidas por rotores de jaula de ardilla o devanados, nos centraremos en los primeros debido a que su utilización es mucho mayor, su fabricación es más sencilla y necesita menor mantenimiento, respecto a las de rotor devanado. Las máquinas de inducción están formadas por una parte fija, el estator, y una parte móvil, el rotor. Entre ambas partes existe una zona conocida como entrehierro, que asegura que no existe contacto mecánico entre ellas y en la que existe un campo magnético giratorio. La Figura 1 muestra el modelo de jaula sencilla por fase, de una máquina de inducción trifásica con pérdidas en el circuito

magnético y la Figura 2 muestra el modelo de doble jaula.

3. Técnicas de estimación de parámetros

Aller en [1] parte de los ensayos de vacío y rotor bloqueado para determinar los valores iniciales de los parámetros de la máquina. Este método necesita la medición directa de la resistencia del estator y de las potencias consumidas en cada ensayo. Akbaba [2] propone una relación constante entre X_{sd} y X'_{rd}, además asume Rs, X_{sd} y R_{fe} constantes para cualquier punto de funcionamiento, los parámetros restantes los estima con relaciones entre ellos. Haque [3] realiza una adaptación a la técnica de Pereira [4], utilizando el modelo exacto del circuito equivalente de la máquina de inducción, datos de par de arranque, eficiencia y factor de potencia de la máquina a 50%, 75% y 100% de carga nominal. Para esta técnica se necesita la medición de la eficiencia y el factor de potencia a media y carga completa, además de una relación fija entre el par de arranque y el par nominal. Existen otros métodos como el de Natarajan et al [5], con la misma metodología o estudios como el de Córcoles et al [6] que demuestra la existencia de infinitos valores para estos parámetros que satisfacen matemáticamente las ecuaciones del circuito equivalente, en régimen permanente. La técnica desarrollada en este trabajo toma los valores conocidos de catálogo y los aspectos constructivos de la máquina, para estimar el valor de los parámetros con técnicas de aproximación de comportamiento, mejorando la relación par-velocidad de la máquina, frente a otras técnicas de estimación paramétrica.

4. Algoritmo propuesto

La técnica mencionada se implementa en un algoritmo de estimación de parámetros que realiza iteraciones para minimizar el error que se obtiene entre vectores de datos teóricos calculados y dos patrones de comportamiento generados por el mismo algoritmo. Estos patrones de comportamiento se generan con base en los datos de catálogo del fabricante y en los aspectos constructivos de cada máquina. El error se calcula en un número configurable de puntos de funcionamiento y el modelo seleccionado es: rotor de jaula sencilla sin pérdidas en el circuito magnético. Esta metodología toma los valores iniciales de R_s y de R'_r desde los datos de catálogo en punto de funcionamiento nominal; con las características constructivas, curvas NEMA y otros datos de catálogo obtenemos el valor de los parámetros restantes. Estos valores son los datos iniciales del algoritmo, que paralelamente genera dos funciones de aproximación de comportamiento de la máquina, lineal e hiperbólica, como referencia de comparación para la función de minimización de error. Esta minimización aplica la técnica de descenso por gradiente para minimizar el residuo cuadrado del error o LMS. Las aproximaciones generadas se realizan analizando el comportamiento de la máquina en puntos de operación específicos, por ejemplo, cuando la velocidad de la máquina tiende a cero, la función par-velocidad se aproxima a una función hiperbólica y cuando tiende a la velocidad máxima, la misma función se puede aproximar a un comportamiento lineal.

5. Resultados

El algoritmo presentado en este trabajo estima tres conjuntos diferentes de parámetros, que se diferencian por la aproximación utilizada para la minimización de su error. Uno de estos conjuntos se estima sin aproximaciones y los dos restantes con aproximación lineal e hiperbólica. El algoritmo grafica también los resultados de las técnicas de Aller y Haque, con el fin de realizar comparaciones y diferencias entre ellas. También se grafican los errores punto-punto, cuadrático y vectorial, cuyo análisis muestra mejor aproximación al comportamiento real de los tres resultados de este algoritmo y menor error respecto a las técnicas de Aller, Haque y Akbaba. En especial, el análisis vectorial muestra que el error de par máximo es menor, en los tres resultados arrojados por la técnica propuesta, respecto a las técnicas mencionadas; en la técnica de Aller también se nota un gran error de velocidad para el punto de funcionamiento de dicho par.

6. Conclusión

La técnica de estimación de parámetros eléctricos presentada, basada en la minimización del error con referencias de comportamiento aproximado, muestra resultados muy satisfactorios al ser comparada con otras técnicas de estimación, mostrando una mejor aproximación en la curva de comportamiento par-velocidad y mejores resultados en el análisis de errores punto-punto, cuadrático y vectorial. Este análisis se aplicó a una máquina de inducción de 4 polos, 3300 V, 50 Hz, 100 Hp y 1455 m^{-1}.

References

[1] J. M. Aller, "*Métodos para el Análisis y Control Dinámico de la Máquina de Inducción*", Universidad Simón Bolivar, Venezuela, Ene. 1997.

[2] M. Akbaba, "*Improved estimation of induction machine parameters*", Electric Power Systems Research, 65-73, Feb 1995.

[3] M.H. Haque, "Estimation of three-phase induction motor parameters", Electr. Power Syst. Res., *26*, 187-193, 1993.

[4] K. Pereira, "*Induction generators for small hydro plants*", WaterPower Dam Constr, 30-34, Nov 1981.

[5] R. Natarajan and V.K. Misra, "Parameter estimation of induction motors using a spreadsheet program on a personal computer", Electr. Power Syst. Res., *16*,157-164, 1989.

[6] F. Córcoles, "Analysis of the Induction Machine Parameter Identification", IEEE Transactions on Energy conversion, Vol. 17, No.2, June 2002.

[7] L. Guasch, "Efecto de los huecos de tensión en las máquinas de inducción y en los transformadores trifásicos", Ph.D. Tesis, Departament d'Enginyeria Elèctrica. Universitat Politècnica de Catalunya, Ene. 2006.

[8] J. Fraile; "Máquinas Eléctricas" .Vol I, servicio de publicaciones, revista obras públicas, 1992.

Improvement of The Gas Pre-concentrator Characterization Procedure Using Mass Spectrometry

H.Lahlou[1,*], P. Ivanov[2], X. Vilanova[1], E. Llobet [1], X. Correig [1]
[1] DEEEA, Universitat Rovira iVirgili, Tarragona, Spain
[2] Gas Sensors Group, Centre National de Microelectrònica, CNM-CSIC, Bellaterra, Spain
Tel. +34 977 558 764, Fax +34 977 559 605 e-mail: houda.lahlou@urv.cat

Abstract

Since it's difficult to obtain gas sensors sensitivities to low concentration gases (ppb level), pre-concentrators are getting importance in this field. To ensure this function, a characterization technique for the pre-concentrator must be setup. In this paper, Mass spectrometry (MS) is used in this way. It shows some advantages over Gas chromatography/Mass spectrometry (GC/MS) techniques in the sense that it allows at the same time to evaluate quantitatively and qualitatively the response of the gas concentrator in real time depending, for example, on the desorption heating mode. This information will be useful in the future to adapt the response of the gas concentrator to the one of a given gas sensor taking into account its response time and detection limit.

1. Introduction

Actually, some toxic gases present at trace concentration only can be identified when a suitable gas concentrator is coupled with the gas sensor.

We have already used GC/MS technique to quantify successfully the response of gas concentrators [1]. The problem we found is that it's not possible to characterize the desorption properties of the preconcentrator as a function of the voltage ramp applied to the heater. As a consequence, it's not possible to know whether the desorption function of the preconcentrator does match with the response of the gas sensors. In the present work, our concentrator is characterized by Mass Spectrometry. This technique allows us to measure on-line the desorption of gases in the preconcentrator in function of time. In our case, we used benzene as a target gas. We will detail the setup of the new characterization procedure of the pre-concentrator and analyze the first results on the influence of heating desorption mode on the behavior of the response of the gas concentrator.

2. Experimental

2.1. Pre-concentrator fabrication

The pre-concentrator has been fabricated from a (1 cm x 1 cm) alumina substrate with a screen printed Platinum heater. Carbopack X (Supelco) has been used as adsorbent. The pre-concentrator was housed in a Teflon chamber containing electrical contacts to heat the concentrator by joule effect for thermal desorption. The Teflon chamber was involved inside a characterization circuit (Fig.1) connected to the MS.

For making the tests, we used as a reference, a calibrated bottle with 150 ppb of benzene balanced in CO_2 [1].

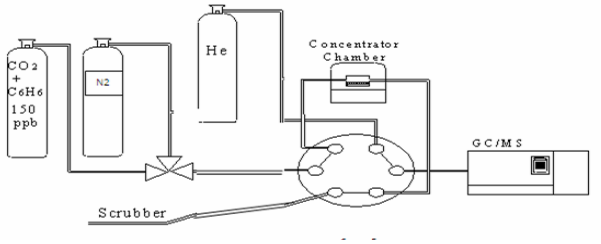

Figure 1: Characterization circuit of the pre-concentrator, the six-way valve being in load position (L.P)

2.2. Setup of the characterization system

A GC/MS-Shimadzu equipped with a Quadrupole (QP5000) has been used. This system is coupled to a six-way valve (Valco Instruments Co. Inc.) that allows the injection of gases (injection position: I.P), the injection mode and time being automatically controlled by software. We've replaced the GC column by a deactivated PR-100052 5 m×0.25 mm ID precolumn (Teknokroma) that only acts as a transfer line from the injector port to the mass detector. We will then be able to visualize in real time the shape of the desorbed peak of the concentrator during the injection to the MS and not in function of the retention time of the column as has been made before using GC/MS technique. This new procedure consists of the following steps:

-Adsorption: The 3-way valve is directed to the open CO_2-bottle direction and the 6-way valve is commutated to the load position (L.P). Thus, the analyte is conducted through the tubes to the concentration chamber to be absorbed. Then it goes outside to the scrubber.

- Desorption and plot of the concentrator response

For starting analysis with the MS, the 6-way valve is commuted to the injection position. Helium passes through the chamber, collects the benzene that remains inside the chamber and tubes and injects it to the MS. When it's completed, we start the desorption of the concentrated benzene by heating the concentrator during 6 min to about 250 ºC

The concentrator response has been displayed as the intensity in counts generated from the mass detector versus time (fig.3.b). We have fixed the m/z 78 to be analyzed, since this m/z is characteristic of benzene.

2.3. Calibration of the Mass Spectrometer

To determine the range of benzene concentrations on which the response of the MS is linear, we made a calibration. We replace the concentrator chamber by a loop, we fill it with the content of calibrated bottles of different concentrations of benzene in CO_2 and we inject the gas to the MS following the previous procedure. Then, we plot the graph of integrated peak areas in function of the concentrations. The response was linear in the range of 70-10000 ppbs (Fig.2). This is effectively the range that interests us for this

application, since benzene (toxic at some ppbs) has to be concentrated from some ppbs to some ppms.

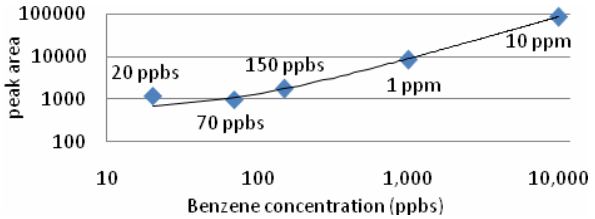

Figure 2: Calibration curve of the MS response toward benzene

2.4. Quantification of the concentration factor

By working in the range of 70 ppbs-10 ppms, the concentration of the desorbed analyte will be proportional to the integrated area of the desorption peak.

To establish a reference peak, the concentrator chamber (containing an uncoated alumina substrate) is filled with benzene from the calibrated bottle. Then, this volume is injected directly to the MS using the same helium flow as for desorption. The area of this peak will be proportional to the initial concentration of the bottle used. By this way, the concentration factor can be calculated as the ratio of the analyte and peak areas integration.

3. Results and discussion

For obtaining the following peak, the adsorption was made during 5 min at 200 ml/min from a bottle of 150 ppbs in CO_2, He flow was set to 10 ml/min.

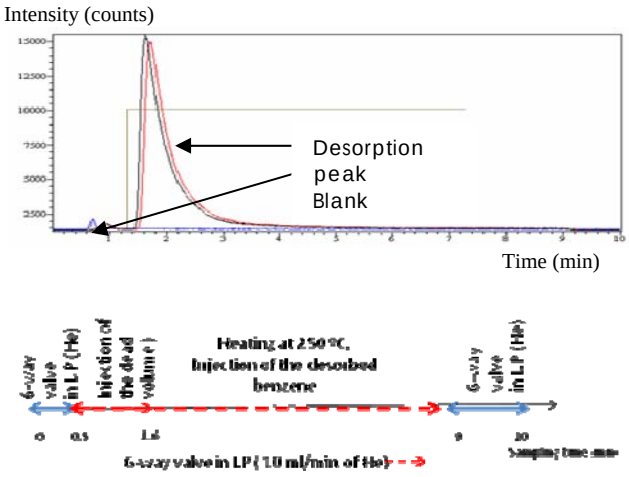

Figure 3: (a) Desorption peak and reference blank obtained from the concentrator toward benzene.(b) Scheme showing the injection modes of the 6-way valve during the display of the MS response

The concentrator factor calculated was around 40. This information, like when using GC/MS characterization, helped us only to compare the adsorption capacity of different pre-concentrators but it didn't ensure if the whole system made by coupling the pre-concentrator with the gas sensor will operate successfully. During the desorption, the analyte is rediluted, so it's possible that the interval of time, during which the concentration of analyte reached the maximum, passes before the sensor response reaches its maximum.

Here, the MS response (Fig. 3) allows also to study how the amount of benzene desorbed from the concentrator is changing in function of time.

So, this procedure allows us to observe that by changing the heating mode of desorption, the peak shape can change.

When using the pulse at 11 V during 6 min (Fig. 4.a), 80 % of the maximum amount of benzene was reached at 0.67 min from heating start. It corresponds to 5171 counts. When using a ramp, the 80 % of the maximum was reached at about 5 min after heating starts (Fig. 4.b). It corresponds only to 3897 counts. In both cases, 80 % of the maximum of concentrated benzene was released when the heater reached about 250 ºC. So, by knowing the response time of the sensor and its detection limit, we can adjust the temperature ramp so as 80 % of the maximum concentration of benzene can be reached at a time much higher than the response time of the sensor.

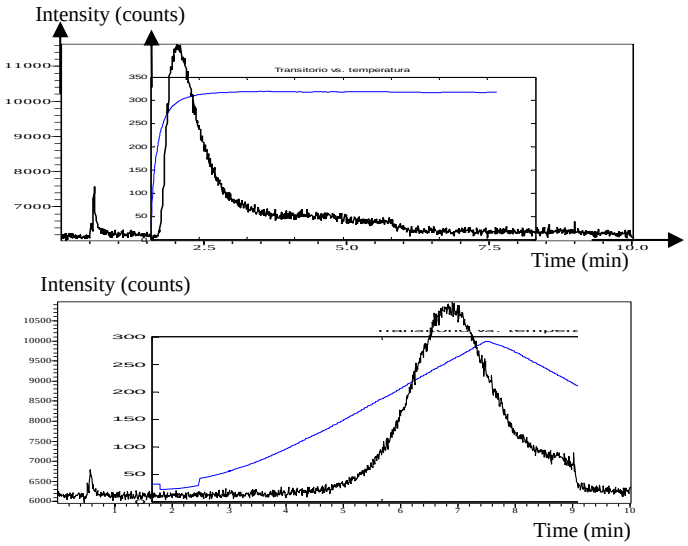

Figure 4: Desorption peak of benzene under heating : a) at 11 V during 6 min. b) At a rate of 1.83 V/min

4. Conclusion

Mass spectrometry allows at the same time a quantitative and qualitative study of the concentrator despite some limitations of the technique. This is useful for the evaluation of the adsorption capacity of a given concentrator or when it will have to be compared with others. The behavior of the pre-concentrator response can be adjusted by using different heating profiles. This information will be useful in the future for a successful operation of the gas concentrator-gas sensor system.

References

[1] F. Blanco et al., *Sensors and Actuators B*, 132 (2008) 90–98

Modelado, Control y Diseño de Sistemas de Potencia para Optimización de Consumo en Pilas de Combustible

C.A. Ramos-Paja, A. Romero, R. Giral
Departamento de Ingeniería Eléctrica, Electrónica y Automática
Universidad Rovira i Virgili, Tarragona, España
Email: carlosandres.ramos@urv.cat

***Abstract*— En este artículo se describe el trabajo desarrollado para optimizar el consumo en pilas de combustible. Este trabajo es desarrollado dentro del programa de doctorado en ingeniería electrónica de la Universitat Rovira i Virgili. El documento describe la motivación y las fases planteadas para su cumplimiento, así como los resultados y conclusiones obtenidas actualmente.**

I. Introducción

Las pilas de combustible son dispositivos que generan energía eléctrica a partir de energía química de forma continua, debido a esto pueden entregar potencia eléctrica en tanto se les suministren reactivos [1]. En este proyecto se han utilizado pilas de combustible tipo PEM para parametrizar y evaluar los sistemas desarrollados, debido a sus ventajosas características de operación (temperatura de operación, eficiencia) y la disponibilidad de prototipos, pero los desarrollos y análisis son válidos para otros tipos de pilas de combustible.

Las pilas de combustible requieren sistemas auxiliares para generar energía de forma eficiente y segura, por lo cual los diferentes fabricantes proveen sistemas autónomos de generación [2]. En la figura 1 se observan los sistemas auxiliares utilizados comúnmente: un sistema de alimentación de oxígeno al cátodo conformado por un compresor de aire y un intercambiador de humedad, un sistema de alimentación de combustible al ánodo conformado por un deposito presurizado de hidrógeno y una válvula de control. Adicionalmente, el circuito del ánodo dispone de una válvula de purga utilizada para remover impurezas y remanentes como gases inertes y partículas de agua, los cuales degradan la potencia producida. Adicionalmente se tiene un sistema de control de temperatura, cuyo flujo de aire es también utilizado para evacuar el hidrógeno excedente en el proceso de purga.

El flujo de aire generado por el compresor se debe controlar con el objetivo de prevenir la aparición del efecto de *agotamiento de oxígeno* en la pila de combustible. Este fenómeno ocurre cuando la proporción entre el oxígeno entregado por el compresor y requerido para generar la corriente demandada es inferior a 1. En este punto, la pila entra en un proceso de rápida degradación y baja producción de potencia, el cual solo puede interrumpirse cesando el funcionamiento de la pila [3]. Adicionalmente, el control del compresor de aire define la potencia neta de salida, determinada por la relación entre la potencia generada por la pila y la consumida por el compresor.

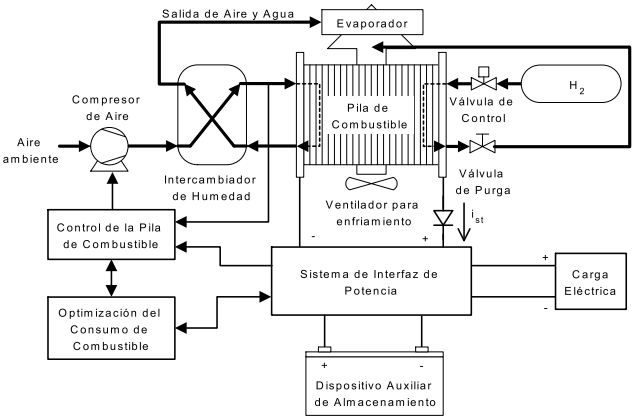

Fig. 1. Topología híbrida basada en pilas de combustible

En este proyecto se propone identificar las condiciones en las cuales la pila de combustible genera la potencia requerida por la carga con el mínimo consumo de combustible. Para esto fue necesario realizar un modelado de la pila de combustible que permitiera estimar estas condiciones. Igualmente fue necesario controlar el compresor y la corriente de la pila para garantizar la estabilidad de las condiciones de mínimo consumo. Esto generó la necesidad de disponer de un sistema auxiliar de energía, para el cual se realizó un análisis de eficiencia de diferentes estrategias de conexión. Estas estrategias requieren sistemas de potencia, cuyo diseño fue soportado por modelos parametrizados y un emulador de pila de combustible desarrollado a partir del modelo diseñado y diferentes etapas de potencia.

II. Modelado

Apartir de modelos físicos [1] [2] y datos experimentales de diferentes prototipos, fue desarrollada una técnica de modelo basada en lógica fuzzy para pilas de combustible. Esta técnica toma en consideración los tres efectos eléctricos más importantes que definen la tensión y potencia eléctrica de la pila: primero, el comportamiento estático definido por las curvas de polarización en diferentes flujos de combustible. Segundo, el efecto de doble capa que determina la constante de tiempo para transitorios de corriente y flujo de combustible. Tercero, el efecto ohmico instantáneo que ocurre en transitorios de corriente.

El modelo resultante considera variaciones de los parámetros de cada efecto en función de la corriente, temperatura y flujo de combustible. Debido a su versatilidad y la generalidad que brindan los parámetros modelados a través de sistemas fuzzy, esta técnica de modelado puede ser aplicada a un amplio rango de sistemas autónomos basados en pilas de combustible. A partir de esta técnica se obtuvo un modelo de un prototipo real, el cual fue validado con datos experimentales presentando un desempeño satisfactorio [4].

El modelo obtenido fue utilizado para analizar el consumo de combustible, así como en el análisis de los sensores requeridos para el desarrollo de estimadores del comportamiento dinámico de la humedad de la membrana en una PEMFC [5]. Igualmente se utilizó en el diseño de emuladores de pilas de combustible y en el diseño de una plataforma modular para monitoreo y caracterización de Pilas de Combustible [6] [7].

III. Sistemas de Potencia

Las pilas de combustible requieren sistemas de potencia para interactuar con cargas eléctricas reales. Así mismo se requieren dispositivos auxiliares de almacenamiento de energía (DAE) que suplan transitorios de alta potencia o que soporten sobrecargas. En la figura 1 se presenta una topología híbrida genérica de pilas de combustible y DAE. En este proyecto se analizaron las topologías típicas de conexión: paralela y serial, evaluando sus ventajas y desventajas para diferentes tipos de cargas eléctricas, y se propuso un criterio de selección [8].

La interfase entre la pila de combustible, el DAE y la carga se realiza a través de convertidores conmutados de potencia. Estos sistemas generan rizados de corriente que deterioran la pila de combustible y reducen la potencia generada. Con el objetivo de evaluar estos dispositivos antes de interactuar con prototipos reales se desarrolló un emulador de pilas de combustible, basado en el procesamiento en tiempo real del modelo y en diferentes etapas de potencia [9] [10]. Este emulador fue validado experimentalmente, presentando un comportamiento satisfactorio en la reproducción de los comportamientos estático y dinámico del prototipo. Así mismo, se evaluaron diferentes topologías de convertidores de bajo rizado para su interacción con pilas de combustible [11].

IV. Control y Optimización

A partir del modelo parametrizado se identificaron los puntos de trabajo óptimos para la pila de combustible, denominados puntos de mínimo consumo, donde la pila entrega la potencia neta requerida por la carga con el mínimo consumo de combustible [12]. Para situar la pila de combustible en estos puntos de trabajo y suplir la demanda de corriente de la carga, se diseñó un sistema de gestión de energía para transiciones suaves de potencia. Con este procedimiento a su vez se garantizó una tensión regulada en la carga, limitando el cambio de potencia requerido a la pila con el objetivo evitar el agotamiento de oxígeno. Se evaluaron controladores clásicos y basados en restricciones, analizando las diferentes configuraciones de DAE para minimizar las pérdidas en los convertidores y el consumo de combustible [8] [13].

V. Conlusiones y Estado del Proyecto

Se han identificado perfiles de control que permiten minimizar el consumo en pilas de combustible. Igualmente se han analizado diferentes topologías híbridas que permiten suplir transitorios de alta frecuencia y evitar agotamiento de oxígeno.

Actualmente se han verificado los perfiles óptimos de control y el modelo matemático, así como el emulador de pilas de combustible. Se encuentra en construcción la topología híbrida para seguimiento de los puntos óptimos ante perfiles de carga con altas frecuencias y bus de carga regulado.

Agradecimientos

Este trabajo fue financiado por el Ministerio de Educación y Ciencia Español bajo el proyecto ENE2005-06934 y la beca FPI BES-2006-11637.

References

[1] A. J. del Real, A. Arce, and C. Bordons, "Development and experimental validation of a pem fuel cell dynamic model," *Journal of Power Sources*, vol. 173, no. 1, pp. 310–324, 2007.

[2] J. Pukrushpan, A. Stefanopoulou, and H. Peng, "Control of fuel cell breathing," *IEEE Control Systems Magazine*, vol. 24, pp. 30 – 46, 2004.

[3] C. Bordons, A. Arce, and A. del Real, "Constrained predictive control strategies for pem fuel cells," *American Control Conference*, pp. 2486–2491, 2006.

[4] C. Ramos-Paja, A. Romero, R. Giral, E. Vidal-Idiarte, and L. Martinez-Salamero, "Fuzzy-based modelling technique for pemfc electrical power generation systems emulation," *IET Power Electronics*, 2008 (Aceptado para publicación).

[5] C. Ramos-Paja, J. Ríos-Torres, A. Romero, R. Giral, and E. Franco-Mejia, "Análisis de los sensores requeridos para el desarrollo de estimadores del comportamiento dinámico de la humedad de la membrana en una pila de combustible," *XIII Simposio de Tratamiento de Señales, Imágenes y Visión Artificial, Colombia*, 2008 (Aceptado para presentación).

[6] J. Ríos-Torres, C. Ramos-Paja, C. Pinedo, A. Romero, and R. Giral, "Plataforma para evaluación y monitoreo del funcionamiento de una pila de combustible," *I Simposium Ibérico de Hidrógeno, Pilas de Combustible y Baterías Avanzadas, España*, 2008 (Aceptado para presentación).

[7] J. Ríos-Torres, C. Ramos-Paja, C. Pinedo, and E. Franco-Mejia, "Implementación de una plataforma modular para monitoreo y caracterización de pilas de combustible," *XIII Simposio de Tratamiento de Señales, Imágenes y Visión Artificial, Colombia*, 2008 (Aceptado para presentación).

[8] C. Ramos-Paja, C. Olalla, C. Bordons, A. Romero, R. Leyva, and R. Giral, "Hybrid topologies analysis for fuel cell qft control design," *XV Congreso Internacional de Ingeniería Eléctrica, Electrónica y de Sistemas INTERCON, Perú*, 2008 (Aceptado para presentación).

[9] C. Ramos, A. Romero, and R. Giral, "Métodos numéricos en la emulación de sistemas de potencia," *Seminario Anual de Automática, Electrónica Industrial e Instrumentación, España*, 2006.

[10] ——, "Fixed-step differential equations solution methods for fuel cell real-time simulation," *International Conference on Clean Electrical Power ICCEP07, Italia*, 2007.

[11] E. Arango, C. Ramos-Paja, J. Calvente, R. Giral, A. Romero, and L. Martínez-Salamero, "Fuel cell power output using a lqr controlled aidb converter," *International Conference on Clean Electrical Power ICCEP07, Italia*, 2007.

[12] C. Ramos, A. Romero, R. Giral, and L. Martinez-Salamero, "Maximum power point tracking strategy for fuel cell power systems," *IEEE International Symposium on Industrial Electronics ISIE-2007*, pp. 2613–2618, 2007.

[13] C. Ramos-Paja, C. Carrejo, A. Romero, E. Vidal-Idiarte, R. Giral, C. Bordons, and M. Milanovic, "Control suave del exceso de oxígeno en una pila de combustible limitando la razón de cambio de la potencia con una rampa de compensación dinámica," *Seminario Anual de Automática, Electrónica Industrial e Instrumentación, España*, 2008 (Aceptado para presentación).

DC, RF and Noise Compact Model for FinFET Including Quantum Effects

B.Nae[1,*], A. Lazaro[1], B. Iñiguez[1]

[1]*Dept. of Electronics, Electrics, and Automatic Engineering,Universitat Rovira i Virgili, 43007 Tarragona, Spain*

[*]Corresponding email: nae.bogden@urv.cat

Abstract

Fin Field Effect Transistors (FinFET) are one of the most promising options for improving the performance of complementary metal-oxide-semiconductor (CMOS) devices into the sub-50 nanometer gate length regime. However, for those dimensions, quantum effects must be considered in order to develop accurate models. This paper studies the influence of the quantum effects on DC, RF and microwave noise for nanoscale FinFETs including non-stationary effects.

Introduction

One of the limiting factors in traditional MOSFET downscaling is the static power consumption due to short channel effects (SCE), including threshold voltage roll-off and subthreshold slope degradation, these effects increasing the off-state leakage current. In multiple-gate (MG) devices, the control of the channel by the gate is stronger than in planar single-gate (SG) MOSFETs. Drain-induced barrier-height lowering (DIBL), threshold voltage roll-off, and off-state leakage can be significantly reduced [1]. This model includes velocity overshoot through a one-dimensional energy-balance model [2,3], the effect of saturation region and the channel modulation length effect and the mobility degradation produced by quantum effects [4].

The purpose of this study is to examine the performance capabilities of FinFET and Triple-gate devices in the RF regime using a simulation study of their small-signal behavior in order to compare their performance with state of-the-art planar RF MOSFETs. Also, a comparison between the drift-diffusion and non-stationary models will be presented.

Model and Results

In order to derive the charge control for FinFETs, we will start to study the charge control in a DG MOSFET as a FinFET limit case when the height is larger than the width. By means of Lambert-function (defined as the solution to equation $W(x)e^{W(x)}=x$), we can write:

$$Q = Q_n W\left(\exp\left(\frac{V_G - V - V_T}{nU_T}\right)\right) \quad (1)$$

where $Q_n=nC_{ox}U_T$, and $n=2$ for $Q_G>>Q_0$, i.e., well above threshold, and n can be interpreted as a fitting parameter with values between 1 and 2. In the case of FinFETs, due to its 3D structure, the charge control given by (1) may be used considering Q_n, V_T and n as unknowns to be extracted from capacitance measurements or numerical simulations. To improve the agreement we propose a new explicit function:

$$Q = Q_{dep} + Q_n W\left(\exp\left(\frac{V_G - V - V_T}{n_{ef}U_t}\right)\right) \quad (2)$$

where Q_{dep} is the depletion charge, and n is replaced by this smoothing function:

$$n_{ef} = \frac{n_{\min}+n_{\max}}{2} + \left(\frac{n_{\max}-n_{\min}}{2}\right)\tanh\left(\frac{V_G - V - V_T + \Delta V_T}{nU_t}\right) \quad (3)$$

where n_{min} is the minimum slope ($n_{min}=1$) and n_{max} is the maximum slope (n_{max} is set to 3 in order to include the top gate charge contributions), ΔV_T takes into account the voltage shift for the top gate charge contributions and n is a smoothing parameter that controls the abruptness of the slope transition between n_{min} and n_{max} and it typically takes values close to 15. In extremely short channel DG MOSFETs and FinFETs the channel is quasi-ballistic, and as a consequence an important velocity overshoot is expected [2]. Using a simplified energy-balance model, the electron mobility is a function of the electron temperature related to the average energy of the carriers. The electron temperature T_e is governed by the following equation:

$$\frac{dT_e}{dx} + \frac{T_e - T_0}{\lambda_w} = -\frac{q}{2k}E_x(x) \quad (4)$$

where the energy-relaxation length is defined as $\lambda_w=2v_{sat}\tau_w$, being τ_w the energy relaxation time, and v_{sat} the saturation velocity. As an approximation, in the channel linear region we can assume that the lateral field is linear from a small value at the source end to the saturation field at $x=L_e$ ($E_x=E_{sat}\cdot x/L_e$). We obtain:

$$I_{DS} = \frac{Wf(V_{gs},V_{DSS})}{L_e + \frac{q\alpha}{2k}\int_0^{L_e} V(\xi)e^{\frac{\xi-L_e}{\lambda_w}}d\xi} = \frac{W}{L_e}\frac{f(V_{gs},V_{DSS})}{1+\gamma_n V_{DSS}} \quad (5)$$

where $\gamma_n = \frac{\mu_{eff}}{v_{sat} L_e} \frac{1}{(1+2\lambda_w/L_e)}$ and V_{DSS} is equal to V_{DS} for non saturated channels (L_e=L) and V_{DSS}=V_{DSsat} for saturated channels.

RF and Noise Modeling

In order to take into account the most important effects, such as non quasi stationary effects, the gate and drain correlation between noise sources, and the tunnelling gate current noise, we use the segmentation method [3,5]. This method is based on splitting the channel in several channel slides. For each channel slide a local small-signal equivalent circuit is derived from the charge control and drain current. The cut-off frequency (f_T) and maximum oscillation frequency (f_{max}) are the most important RF figure merit parameters [6,7,8]. These parameters can be calculated from the small signal equivalent circuit extracted from the Y parameters computed using the active transmission line analysis identifying each branch of the Pi equivalent circuit.

$$f_T = \frac{g_m}{2\pi C_{gs}\sqrt{1+2C_{gd}/C_{gs}}} \approx \frac{g_m}{2\pi(C_{gs}+C_{gd})} \quad (6)$$

$$f_{max} \approx \frac{g_m}{2\pi C_{gs}\sqrt{4(R_s+R_i+R_g)\left(g_{ds}+g_m\frac{C_{gd}}{C_{gs}}\right)}} \quad (7)$$

where C_{gs} and C_{gd}, are the gate to source and gate to drain small signal capacitance respectively, including fringing and overlap capacitances, g_m is the gate transconductance, R_i (in series with C_{gs}) takes into account the distributed nature of the MOSFET and g_{ds} is the drain-to-source conductance.

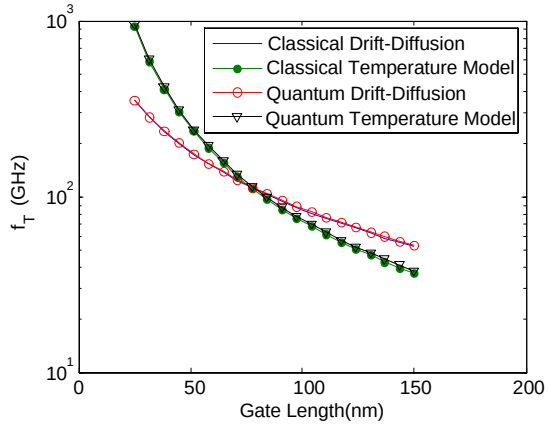

Fig.1. Simulated cut-off frequency f_t versus gate length for FinFET (W_{fin}=10 nm, H_{fin}=30 nm, t_{ox}=1.5 nm, t_{box}=50 nm, V_{ds}=1 V, V_{gs}-V_{TH}=0.5V)

Some results for cut-off and maximum oscillation frequencies and intrinsic noise parameters for drift-diffusion and hydrodynamic using classical and quantum compact charge model are presented in fig.1-3.

As a conclusion, the results show important differences in drain current, f_T and noise performances between drift-diffusion and hydrodynamic models for short gate lengths. These differences are due to the velocity overshoot increasing the transconductance, and the hot-carrier effects in the noise temperature.

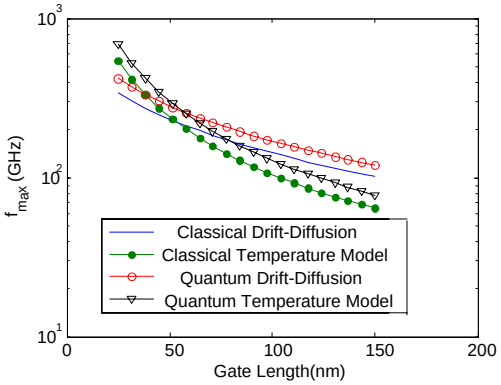

Fig.2. Simulated f_{max} versus gate length for FinFET (W_{fin}=10 nm, H_{fin}=30 nm, t_{ox}=1.5 nm, t_{box}=50 nm, V_{ds}=1 V, V_{gs}-V_{TH}=0.5V)

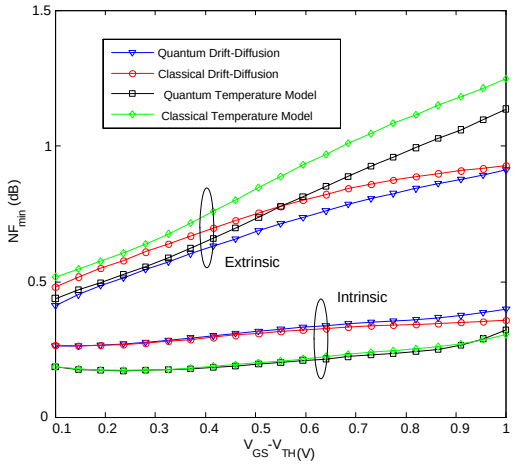

Fig.3. Minimum Noise figure for intrinsic and extrinsic device (W_{fin}=10 nm, H_{fin}=30 nm, t_{ox}=1.5 nm, t_{box}=50 nm, L=50 nm, 100 fingers, V_{ds}=1V) as function of gate overdrive voltage.

References

[1] F. Balestra, S. Cristoloveanu, M. Benachir, J. Brini, and T. Elewa, IEEE Electron Device Lett., 8, 410 (1987)

[2] G. Baccarani, S. Reggiani, IEEE Trans. on Electron Devices, 46, 1656 (1999)

[3] A. Lázaro, B. Nae, O. Moldovan, B. Iñíguez, Journal of Applied Physics, 100, 084320 (2006)

[4] L. Ge and J.G. Fossum, IEEE Trans. on Electron Devices, 49, 287 (2002)

[5] A. Lázaro, B. Iñíguez, Solid-State Electronics, 50, 826 (2006)

[6] J.-P. Raskin, M.-C. Tsung, V. Kilchytska, D. Lederer, D. Flandre, IEEE Trans. on Electron Devices, 53, 1088 (2006)

[7] G. Pailloncy, B. Iniguez, G. Dambrine, J.P. Raskin and F. Danneville, Solid-State Electronics, 48, 813 (2004)

[8] A.Lázaro, B.Nae, et al. Journal of Applied Physics 103, 084507 (2008)

High Frequency and Noise Model of Gate-All-Around MOSFET Transistors

B.Nae[1,*], A. Lazaro[1], B. Iñiguez[1]
[1]*Dept. of Electronics, Electrics, and Automatic Engineering,Universitat Rovira i Virgili, 43007 Tarragona, Spain*
[*]Corresponding email: nae.bogden@urv.cat

Abstract

The surrounding gate (SGT) MOSFET is one of the most promising candidates for the downscaling of CMOS technology toward the sub-50 nanometre channel length range, since the surrounding gate architecture allows an excellent control of the channel charge in the silicon film, reducing short channel effects. However, for those dimensions quantum effects must be considered in order to develop accurate compact models useful for circuit simulations. We study the influence of the quantum effects on DC, RF and microwave noise for nanoscale SGT transistors including nonstationary effects. RF and noise performances are calculated using the active transmission line method. A comparison between classical and quantum charge control, and between drift-diffusion and hydrodynamic models is carried out.

Introduction

Based on a previous study [1], where we presented an analytical method for RF and noise modelling applied to SG and DG SOI MOSFET devices, we extend the model SGT devices, and the DC, RF and High Frequency Noise models will be presented. The model includes velocity overshoot through a one-dimensional (1D) energy-balance model [2,3], the effect of the saturation region, the channel modulation length effect and the mobility degradation produced by quantum effects.

The model is based on the concept of channel segmentation [1,3], and a includes the formulation for drift-diffusion and temperature (hydrodynamic) transport models. High frequency performances are analyzed through the use of analytical expressions of the cut-off frequency f_T and maximum frequency of oscillation f_{max}, and noise properties of the devices are discussed.

Model and results

Using a novel centroid model, a classical inversion charge model [4] has been improved, in order to include quantum effects [5], and the total charge Q is obtained (1), where C_{TOTAL} is given by:

$$\frac{1}{C_{TOTAL}} = \frac{1}{C_{Oxide}} + \frac{1}{C_{Semiconductor}} \qquad (2)$$

where

$$C_{Oxide} = \frac{\varepsilon_{ox}}{R \cdot \ln\left(1 + \frac{t_{ox}}{R}\right)} \qquad (3)$$

and

$$C_{Semiconductor} = \frac{\varepsilon_{Si}}{\left(R - z_1\right) \ln\left(1 + \frac{t_{ox}}{R}\right)} \qquad (4)$$

Note that if C_{TOTAL} is replaced in (1) by C_{Oxide}, a classical charge control model is obtained.

Concerning the channel current, we expect to use the same expression as in DG MOSFETs [3], because the type of confinement in SGT and the shape of the first eigenfunction is qualitatively similar to DG devices, with $t_{si}=2R$ and the effective thickness $t_{si,eff}$ replaced by $2R_{eff}$ obtained from the centroid z_I, where:

$$\frac{1}{z_1} = \frac{1}{a + 2bR} + \frac{1}{z_{I0}}\left(\frac{N_I}{N_{I0}(R)}\right)^n$$,with a=0.55 nm, b=0.198, z_{I0} =5.1 nm, n=0.75 and

$$N_{I0}(cm^{-2}) = 8.26 \times 10^{12}\, cm^{-2} - 4.9 \times 10^{18}\, cm^{-3} \times R\,(cm) \qquad (5)$$

The channel current has the following expression:

$$I_{DS} = \frac{Wf(V_{gs}, V_{DSS})}{L_e + \frac{q\alpha}{2k}\int_0^{L_e} V(\xi) e^{\frac{\xi - L_e}{\lambda_w}} d\xi} = \frac{W}{L_e}\frac{f(V_{gs}, V_{DSS})}{1 + \gamma_n V_{DSS}} \qquad (6)$$

where $\gamma_n = \frac{\mu_{eff}}{v_{sat} L_e}\frac{1}{\left(1 + 2\lambda_w / L_e\right)}$ and V_{DSS} is equal to V_{DS} for non saturated channels ($L_e=L$) and $V_{DSS}=V_{DSsat}$ for saturated channels.

$$Q = C_{TOTAL}\left(-\frac{2C_{TOTAL}V_{th}^2}{Q_o} + \sqrt{\left(\frac{2C_{TOTAL}V_{th}^2}{Q_o}\right)^2 + 4V_{th}^2 \ln^2\left(1 + \exp\left(\frac{V_{GS} - V_T + \Delta V_T - V}{2V_{th}}\right)\right)}\right) \qquad (1)$$

RF and Noise Modeling

Fig.1-2 present some simulated results for the most important RF figure merit parameters, the cut-off frequency (f_T) and maximum oscillation frequency (f_{max}). Fig.3 shows the intrinsic and extrinsic noise figure for SGT (R=5 nm, t_{ox}=1.5 nm, V_{ds}=1 V, V_{gs}-V_{TH}=0.5V) at 10 GHz calculated using the drift-diffusion and temperature models. Fig.4 shows the frequency dependence of the noise performance, for the same SGT, and compares the two transport models.

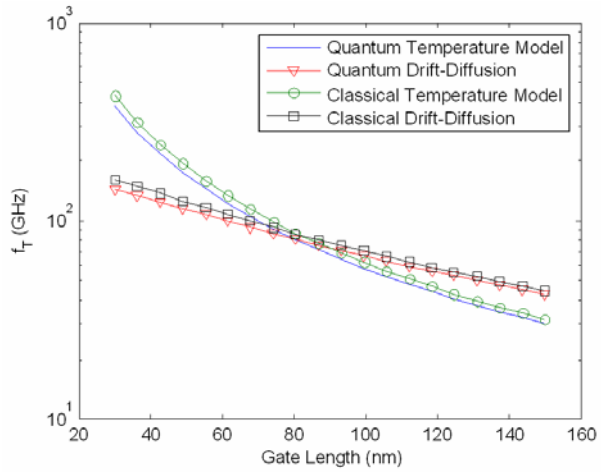

Fig.1. Transition frequency f_T as function of gate length. Radius R=5 nm, V_{GS}-V_{TH}=0.5V, V_{DS}=1V

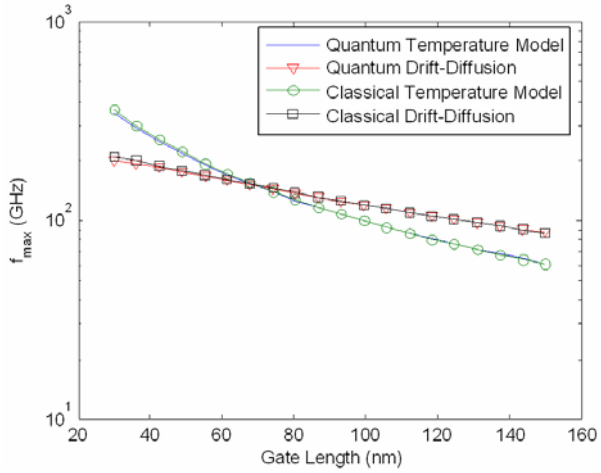

Fig.2. Maximum Oscillation frequency f_{max} as function of gate length. Radius R=5 nm, V_{GS}-V_{TH}=0.5V, V_{DS}=1V

As a conclusion, the obtained results show important differences in f_T, f_{max}, and noise performances between drift-diffusion and hydrodynamic models for short gate lengths. These differences are due to the velocity overshoot that increases the transconductance, and hence, f_T and f_{max} values. Also, significative difference have been observed in f_{max} and minimum noise figure between classical and quantum models. The electronic temperature transport model predicts higher noise temperature in saturation bias region than the classical

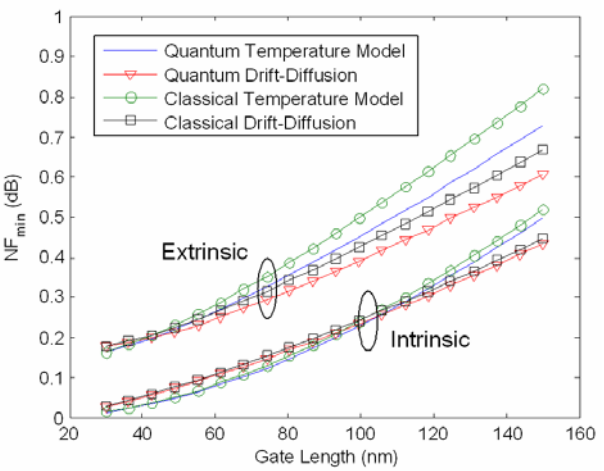

Fig.3. Intrinsic and extrinsic Minimum Noise Figure NF_{min}(dB) as function of gate length. Radius R=5 nm, V_{GS}-V_{TH}=0.5V, V_{DS}=1V

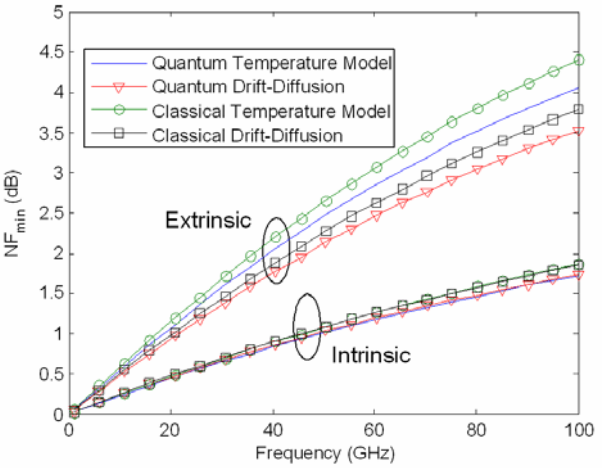

Fig.4. Intrinsic and extrinsic Minimum Noise Figure NF_{min}(dB) as function of frequency. Gate length L=100 nm, Radius R=5 nm, V_{GS}-V_{TH}=0.5V, V_{DS}=1V

relation between carrier temperature and electric field, resulting in a higher noise figure. However, for gate lengths shorter than about 50-60 nm the increase of f_T due to velocity overshoot compensates the channel temperature increment finally resulting in a lower noise figure. The simulated results show the limiting effect of parasitics in SGT RF and noise performances.

References

[1] Lazaro A, Iñiguez B, Solid-State Electronics, 50, 826–42 (2006)

[2] G. Baccarani, S. Reggiani, IEEE Trans. Electron Devices, 46, 1656 (1999)

[3] A. Lázaro, B. Nae, O. Moldovan, B. Iñíguez, Journal of Applied Physics, **100**, 084320 (2006)

[4] B. Iñiguez, D. Jiménez, J. Roig, H. A. Hamid, L. F.Marsal, and J. Pallares, IEEE Trans. Electron Devices, **52**, 8, 1868–1873 (2005)

[5] J. B. Roldán, Andrés Godoy, Francisco Gámiz, M. Balaguer, IEEE Trans. Electron Devices, **55**, 1 (2008)

Design of an optical switch based on 2D tunable photonic crystals

Joaquín COS, Lluís F. MARSAL, Josep PALLARÈS and Josep FERRÉ-BORRULL

Nanoelectronic and Photonic Systems Group
D.E.E.E.A., Universitat Rovira i Virgili, Avda. Països Catalans 26, 43007 Tarragona, Spain
lluis.marsal@urv.net.

Abstract

A theoretical study of 2D photonic crystals composed of anisotropic materials is presented. We analyzed the TE and TM modes for a 2D silicon photonic crystal with liquid crystal scatterers in the XY plane and a 2D liquid crystal photonic crystal with silicon scatterers in the XY plane. The analysis of the structures has been made by plane-wave expansion method. Changes of the photonic band structures by varying liquid crystal's optical axis orientation in the XY plane are discussed. These structures can be used to design electrooptical devices such as switchers.

1. Introduction

Photonic crystals (PCs) are periodic dielectric or metal-dielectric synthetic nanostructures designed to affect the propagation of electromagnetic waves in the same way as the periodic potential in semiconductor crystals affects the electron motion by defining allowed and forbidden energy bands. Since first proposed [1], [2] their potential scientific and technological applications have inspired great interest among researchers. Photonic crystals offer an important opportunity to design new optical devices and hold a great potential for many significant applications, such as semiconductor lasers and solar cells, high quality resonator and filters, optical fibers.

In the last decade many efforts have been spent towards tuning the properties of photonic crystals in order to design switchable or dynamical devices. Several structures combining photonic crystals with liquid crystals (LC) materials have been proposed [3] where the refractive index can be varied either by changing the operating conditions (i.e. temperature) or applying an external field [4].

In this work we present a study and discussion of two 2D silicon photonic crystals infiltrated by liquid crystal. We base the analysis on Plane-Wave Expansion (PWE) method for TE and TM modes

2. Numerical method

Let us consider a 2D photonic crystal with periodicity in the x-y plane and uniform refractive index variation in the z direction. The 2D photonic crystals we study in this work are composed of an isotropic component (Silicon) and a uniaxial anisotropic component (E7 liquid crystal).

We want to study structures where the TE and TM polarizations can be decoupled. For this, it is important to have the anisotropic materials in an orientation such that the polarizations can be decoupled and that the direction of the extraordinary axes influences the photonic bands. Following [5], Maxwell's equations can only be decoupled in two cases: i) when the optical axis is oriented along the rods of the 2D photonic crystal, and ii) when the optical axis is perpendicular to the rods. Furthermore, only in the second case, the direction of the optical axis influences the photonic band structure. In this second case, the dielectric tensor can be decomposed into two parts, one for the x-y plane, (ε_r) and one for the z direction ($\varepsilon_z=\varepsilon_o$).

$$\varepsilon_r(\mathbf{r}) = \begin{pmatrix} \varepsilon_{11}(\mathbf{r}) & \varepsilon_{12}(\mathbf{r}) \\ \varepsilon_{21}(\mathbf{r}) & \varepsilon_{22}(\mathbf{r}) \end{pmatrix} = \begin{pmatrix} \varepsilon_o sin^2\alpha + \varepsilon_e cos^2\alpha & (\varepsilon_o - \varepsilon_e)\cdot cos\alpha \cdot \sin\alpha \\ (\varepsilon_o - \varepsilon_e)\cdot cos\alpha \cdot \sin\alpha & \varepsilon_o cos^2\alpha + \varepsilon_e sin^2\alpha \end{pmatrix}, \quad (1)$$

where α is the angle between the optical axis and the x-axis.

Without coupled modes we obtain the following eigenequations for the TE and TM polarizations, respectively:

$$\nabla_{xy} \times \varepsilon_r^{-1}(\mathbf{r}) \times \nabla_{xy} \times \mathbf{H}_z(\mathbf{r})\hat{\mathbf{z}} = \hat{\omega}\mu_0\varepsilon_0\mathbf{H}_z(\mathbf{r})\hat{\mathbf{z}}, \quad (2)$$

$$-\varepsilon_o^{-1}(\mathbf{r})\left(\frac{\partial^2}{\partial x^2} - \frac{\partial^2}{\partial y^2}\right)\mathbf{E}_z(\mathbf{r}) = \omega^2\mu_0\varepsilon_0\mathbf{E}_z(\mathbf{r}). \quad (3)$$

where $\nabla_{xy} = \hat{\mathbf{x}}\cdot\partial/\partial x + \hat{\mathbf{y}}\cdot\partial/\partial y$. From Eqs. 2 and 3 it can be inferred that, for this configuration, optical axis orientation of liquid crystal only influence TE modes. For this reason, all of our analyses are centered in TE modes.

As we comment on the previous section, we analyze structures by means of PWE method. In order to illustrate the application of this method we consider triangular lattice and analyze it with PWE this method. Applying Bloch theorem to Equation 2 we can obtain the eigenequation for TE polarizations:

$$\sum_{\mathbf{G}'} (\mathbf{k}+\mathbf{G}) \bullet \varepsilon^{-1}_{r\mathbf{G}\mathbf{G}'} (\mathbf{G}-\mathbf{G}') \bullet (\mathbf{k}+\mathbf{G}') \cdot H_{z,\mathbf{k}}(\mathbf{G}') = (\omega/c)^2 \cdot H_{z,\mathbf{k}}(\mathbf{G}), \quad (4)$$

Due to the anisotropy of the liquid crystal and its influence on the TE polarization, the Irreducible Brillouin Zone (IBZ) usually considered for isotropic 2D photonic crystals with triangular lattice it is not sufficient to represent the whole First Brillouin Zone (FBZ). We propose calculating the bands along the **k** in the main high symmetry directions of the First Brillouin Zone. With this aim we have divided the upper half of the FBZ in sets of **k** points denominated BZ_{30}, BZ_{60}, BZ_{90}, BZ_{120}, BZ_{150}, and BZ_{180}, as it is shown in Figure 1.

Figure 2 shows for a silicon photonic crystal with a triangular lattice of circular holes infiltrated with liquid crystal for the TE polarization the values of the lower and upper edge of the photonic band gap between 1st and 2nd bands, obtained from each of the sets. Since the maximum for the 1st band is at point Γ, its value is almost independent of the LC optical axis orientation. Instead, the minimum of the 2nd band is strongly dependent on α. The figure shows only the minima obtained from the BZ_{30}, BZ_{90} and BZ_{150}, since their values are the same as those obtained from the BZ_{60}, BZ_{120} and BZ_{180}, respectively. Figure 2 also shows the resulting gap-to-midgap ratio.

Figure 3 shows the gap-to-midgap ratio for the inverse structure, that is, a photonic crystal of silicon cylinders surrounded by liquid crystal. In this case, due to the closing of the gap for a range of angles it can be employed as electrooptical switch.

3. Conclusions

We have studied a structure based on silicon photonic crystal and liquid crystal that allows a completely tuning of a band gap. By means of the plane-wave expansion method we have analyzed the TE and TM modes. In particular, we have applied PWE method for a silicon photonic crystal with a triangular lattice of liquid crystal infiltrated holes and a liquid crystal photonic crystal with a triangular lattice of silicon rods. For these structures, the gap width has a 60º periodicity on the LC's optical axis orientation. Maximum gap is obtained for LC's optical axis orientation angles multiples of 60º and minimum for odd multiples of 30º. By means of a LC photonic crystal with silicon rods we have designed an optical switch, where for a range of LC's optical axis orientation the gap disappears.

Acknowledgements

This work was supported by the Spanish Ministry of Science under Grant number TEC2006-06531. J. Ferré-Borrull acknowledges the Ramon y Cajal fellowship from the Spanish Ministry of Science and Technology.

References

[1] S. John, *Phys. Rev. Lett.* **58** 2486, 1987.
[2] E. Yablonovitch, *Phys. Rev. Lett.* **58** 2059, 1987.
[3] K. Busch and S. John, *Phys. Rev. Lett.* **83** 967, 1999.
[4] S. M. Weiss, *et al*., *Opt. Express* **13** 1090, 2005.
[5] G. Alagappan *et al., J. Opt. Soc. Am. A* **23** 2002, 2006.

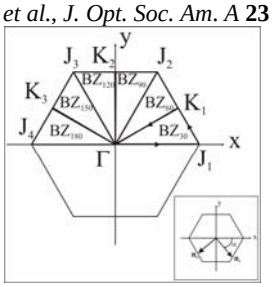

Fig.1. *Definition of the BZ sets for the studied photonic crystals. (Inset) LC optical axis orientation.*

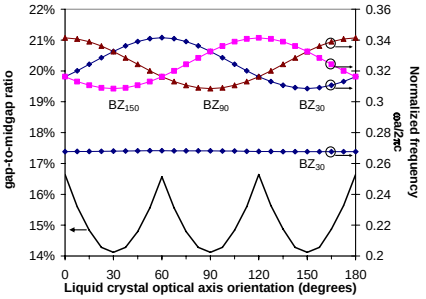

Fig.2. Maximum and minimum normalized frequencies for the 1st and 2nd TE modes, and corresponding gap-to-midgap ratio versus LC optical axis orientation

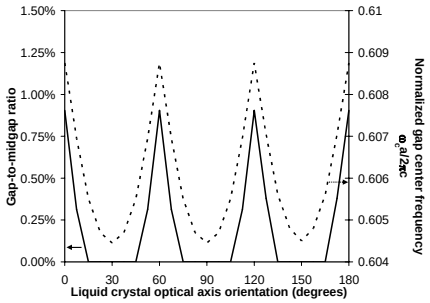

Fig.3. *Gap-to-midgap ratio (solid line) and gap center (dashed line) between 4th and 5th TE modes versus LC optical axis orientation.*

Enhancement of sensitivity in gas chemoresistors based on surface functionalized carbon nanotubes decorated with metal nanoclusters

R. Leghrib[1*], A. Felten[2], J.J. Pireaux[2], E. Llobet[1]

[1]*MINOS*, Departamento de Ingeniería Electrónica I Automatica, ETSE, Universidad Rovira i Virgili, Avda. Países Catalans, 26, 43007, Tarragona, Spain
[2]LISE, Université de Namur, B-5000, Namur, Belgium

Radouane.leghrib@urv.cat Tel : 977 25 65 72, Fax : 977 55 96 05

Abstract

Untreated multi-wall carbon nanotubes were deposited by drop coating method onto micro-hotplates with integrated arrays of micro-sensors. Nanotubes were then functionalized and decorated by metal evaporation. The chips were encapsulated and used to detect several hazardous gases. The responsiveness of the sensors was investigated.
This inverse method of deposition shows advantageous Results for sensing at room temperature.

1. Introduction

Because of the interesting physical and chemical properties of carbon nanotubes, they were highly used in different fields: catalyst supports in heterogeneous catalysis, electronic devices, field emitters, sensors, gas storage media and molecular wires for next generation of electronic devices [1].
The large surface area and the detection at room temperature make from the carbon nanotubes ideal gas detection.
The functionalization and the decoration of the nanotubes make them more powerful for using in gas detection.
In this work, we have found a new process to deposit the carbon nanotubes onto the silicon micro-machined membrane. The new procedure has shown that is useful and reproducible to make sensors more sensitive at room temperature.

2. Materials

The carbon nanotubes used were multi-wall carbon nanotubes produced by Mercop, the purity higher than 95%. The as provided CNTs were dispersed in acetone and then the solution was drop coated onto the electrode area of the integrated micro-hotplate.
The deposited carbon nanotubes were functionalized in a home-made chamber using inductive coupled plasma at the RF frequency of 13.56 Mhz then were decorated by metal nanoclusters using a metal thermal evaporation method.

3. Experiment

We dispersed the untreated carbon nanotubes in the acetone as organic vehicle. The solution was placed in an ultra-sonication bath during several minutes to achieve an adequate homogenization.
The resulted solution was drop coated onto the one hundred sensors dies; they were kept at room temperature for several minutes to evaporate the acetone and then were annealed at 250ºC during 3 hours. The as deposited carbon nanotubes were functionalized by oxygen plasma and then decorated by metals using a thermal evaporation method. Finallly, the chips were encapsulated in standard TO-8 packages.
The sensors were placed in a testing chamber where the contaminants were introduced. The tests of the sensors were assisted by an Agilent multimeter and a personal computer to record the signal from the sensors. This signal consisted of the change in resistance of the metal decorated carbon nanotube active layers.
The morphology of the different active layers was investigated by SEM analysis.

4. Results

According to the obtained results, we found that this deposition method helps us to overcome the drawbacks found in our initial works (i.e. the removal of metal nanoclusters from the surface of the carbon nanotubes due to harsh deposition conditions). In particular, it is shown that by avoiding the thermal treatment of the metal decorated carbon nanotubes (this treatment is used to evaporate the solvent used to deposit the active materials) can highly improve the sensitivity towards some toxic gases. In this work, gold decorated MWNTs showed interesting results in the detection of NO_2 at room temperature. Before, no response was obtained to this gas operating the sensors at room temperature.

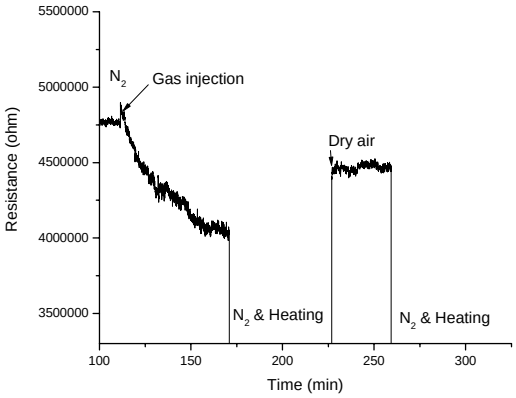

Fig.1. the resistance changes toward the NO_2 test by Au-decorated MWNTs active layer.

We have tested other gases such as ethylene, benzene but the sensors cannot detect them thanks to the high resistance value of the sensors. In this work we had a problem, which consists in a bad definition of the deposition area. This results in a too little amount of material onto the electrode area (see fig.2), which makes the sensors too resistive and affect the sensitivity towards some gases. This is especially true when a week interaction occurs between the gas and the active layer.

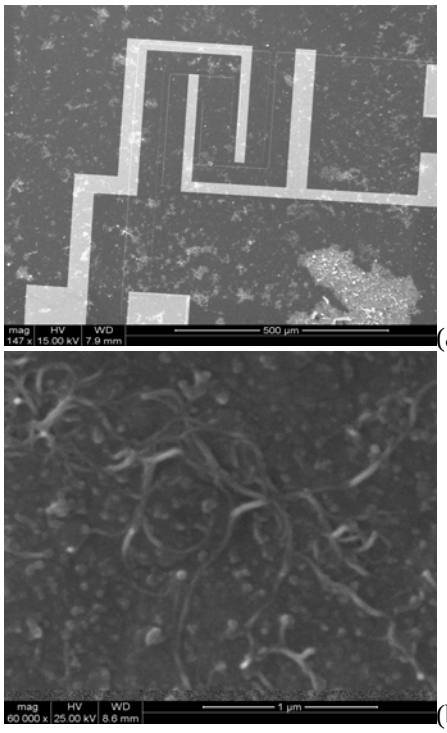

Fig.2. The metal decorated MWNTs deposited over the sensor substrate. (a) General view of the electrode area (b) close view within the electrode area.

5. Conclusions

The new procedure to fabricate gas sensors showed good results concerning the sensitivity of the sensor. The remaining problem is the high value of the sensor resistance that affects the sensitivity toward other toxic gases. Although, this makes the sensors more selective towards oxidizing gases such as NO_2.

Acknowledgment:
This work is financially supported by Nano2Hybrids (EC-FP6-STREP-033311).

References

[1] A. Star, et al, J. Phys. Chem. B, 110, pp. 21014-21020, Aug. 2006.

Fabrication of Nickel and Cobalt Nanowires Using Home-Made Porous Alumina As Template

A. SANTOS, J. PALLARÉS, J. FERRÉ-BORRULL AND L. F. MARSAL*

Universitat Rovira i Virgili, ETSE-DEEEA,Av. Països Catalans 26, 43007 Tarragona - Spain

**E-mail:lluis.marsal@urv.cat Tel.: +34 977 55 96 25*

Abstract

We report a way to produce arrays of Ni and Co nanowires in anodic porous alumina membranes by means of DC electrodeposition. Environmental scanning electron microscopy (ESEM) analysis showed both nanowires diameter and longitude. The surface topography of the template was studied using atomic force microscopy (AFM) and ESEM as well. Finally, the nanowires microstructural characteristic was analyzed by x-ray diffraction (XRD) in order to find their crystalline phase.

1. Introduction

Scientists have made a lot of efforts in order to improve the fabrication process of porous alumina membranes (PAMs) for a long time [1]. Since the two-step anodization process was used for the first time [2], many research groups have studied this process and new ways to produce PAMs have been come out [3]. Previous studies have established the relationship between PAM properties and the work parameters (acid, applied voltage, temperature, anodizing time, etc.) [4-6]. This fact has allowed to us produce PAMs controlling relatively their morphology. Therefore, we can adapt home-made PAMs to later applications. One of these applications is to use PAMs as template in order to fabricate nanostructures as nanowires, nanotubes and nanorods. Technological applicability of metallic submicron structures has generated tremendous interest in recent years due to their optical and electrical properties and great potential for applications in quantum devices [7-9].

2. Experimental part

Aluminum substrates (High purity aluminum (99.999%) foils from Goodfellow Cambridge Ltd.) were used to produce home-made PAMs by typical two-step anodization process [2]. Firstly, these substrates were pre-treated in order to improve their physical properties as surface roughness and crystalline phases. The foils were annealed in nitrogen (N_2) environment at 400ºC for 3 hours. Afterwards, they were electropolished in a mixture of EtOH and $HClO_4$ 4:1 (v:v). Once the samples were washed with distilled water and dried, a two-step anodization was performed on the aluminum surface using oxalic acid (0.3M). Both first and second step were carried out using a potenciostatic regime with different potentials, which depend on the used acid. When the first anodization stage was finished, a film of alumina with disordered pores was obtained. Then, this thin film was removed from the aluminum substrate by wet chemical etching in a mixture of phosphoric acid (0.4M) and chromic acid (0.2M) at 70ºC during the same time of first step (about 30 minutes). In this way, we produced a pre-pattern on aluminum surface. Subsequently, the second step consisted in repeating the same conditions used in the first step but varying the etching time to obtain a thicker film (approximately 8μm/h). A PAM with ordered pores resulted from the second step Figure 1 shows the AFM image of the resulting membranes. After the anodization process was finished, the oxide barrier layer of the pore bottom tips was removed. Afterwards, we proceeded to electrodeposited Ni and Co inside PAMs in order to produce nanowires of these metals by template method. The upper side of the membranes was placing in contact with an electrolyte solution containing Ni sulphate ($NiSO_4$) and Ni chloride ($NiCl_2$) as nickel source and Co sulphate ($CoSO_4$) as cobalt source. Both aqueous solutions used boric acid (H_3BO_3) as stabilizer. After a preliminary immersion of the membrane in the same bath during certain time (15 minutes), the electrodeposition was performed applying a constant voltage profile. Finally, to characterize these samples after the electrodeposition process, they were immersed in a mixture of phosphoric acid (0.4M) and chromic acid (0.2M) at 70ºC during several minutes in order to dissolve partially the alumina template. Figure 2 shows the ESEM images of the resulting Nickel and Cobalt nanowires, whose diameters and longitudes were 60nm and 24μm, respectively. These measurements reply the pore template dimensions. Figure 3 shows their corresponding XRD analysis.

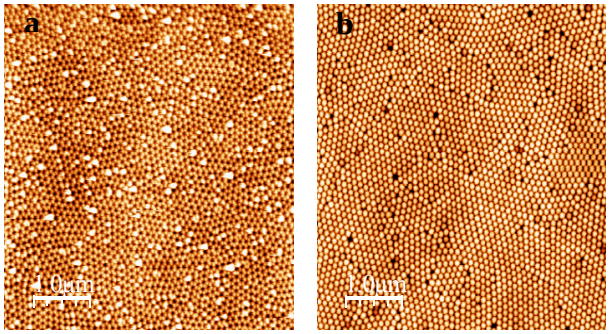

Figure1: AFM image of porous alumina membrane. a) Top. b) Bottom.

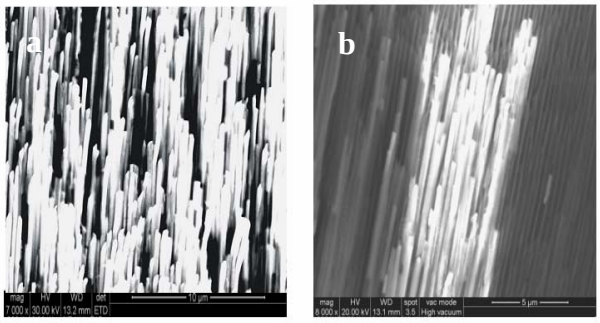

Figure2: ESEM images of metallic nanowires. a) Nickel nanowires. b) Cobalt nanowires.

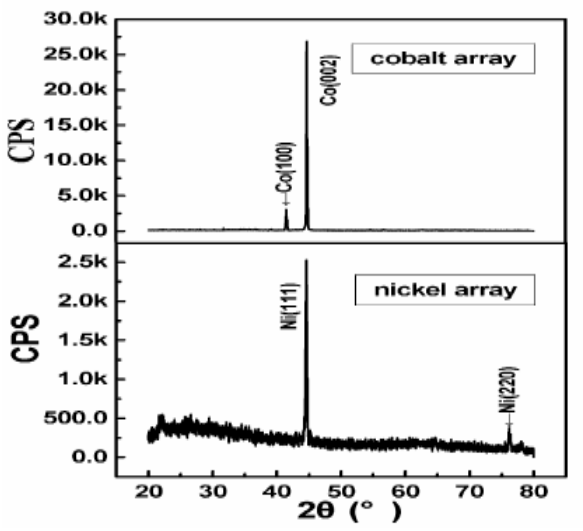

Figure3: XRD patterns of nickel and cobalt nanowires arrays.

4. Conclusions

Self-ordered porous alumina membranes have been fabricated, characterized, analyzed and used as template in order to produce nickel and cobalt nanowires, which were characterized too. The nanowires were obtained with high purity because there are not diffraction peaks of their oxides. In addition, the preferentially oriented growth was mainly along the (111) crystal direction for Ni and the (002) crystal direction for cobalt, what may be attributed to the confined growth of the nanowires within the porous alumina membrane.

Acknowledgements

This work was supported by the Spanish Commission of Science and Technology (MEC) under grant number TEC2006-02038 and CONSOLIDER HOPE project CSD2007-00007. J. Ferré acknowledges the Ramón y Cajal fellowship from the Spanish Ministerio de Ciencia y Tecnología.

References

[1] F. Keller, M. S. Hunter and D. L. Robinson, J. Electrochem. Soc., 100 (1953) 411
[2] H. Masuda, K. Fukuda, *Science*, 268 (1995) 1466
[3] K. Nielsch, R. B. Wehrspohn, J. Barthel, J. Kirschner, U. Gösele, S. F. Fischer, and H. Kronmüller, *Appl. Phys. Lett*., 79 (2001) 1360-1362
[4] G. Che, B. B. Lakshmi, E. R. Fisher, C. R. Martin, *Nature,* 393 (1998) 346
[5] Y. Du, W. L. Cai, C. M. Mo, J. Chen, L D. Zhang and X. G. Zhu, *Appl. Phys. Lett*., 74 (1999) 20
[6] L. F. Marsal, L. Vojkuvka, J. Ferré-Borrull, T. Trifonov, and J. Pallarès phys. stat. sol. (c) 4, No. 6, (2007)1918-1922
[7] A.M. Morales and C.M. Lieber *Science* (1998) 279 208
[8] [8] X. Duan, J. Wang and C.M. Lieber *Appl. Phys Lett.* (2000) 76 1116
[9] [9] E. Ko , J. Choi, K. Okamoto, K. Tak and L. Lee *ChemPhysChem* (2006) 7 1505

Fabrication of polymer micro- and nanostructures using porous templates

R. Palacios[1], P. Formentín[1], T. Trifonov[2], J. Ferré-Borrull[1], J. Pallarés[1], A. Rodríguez[2], R. Alcubilla[2] and L. F. Marsal[1]

[1]Departament d'Enginyeria Electrònica, Elèctrica i Automatica, Universitat Rovira i Virgili, Av. Països Catalans 26, 43007 Tarragona, Spain
[2]Departament d'Enginyeria Electrònica, Universitat Politècnica de Catalunya, Edifici C4, Campus Nord,c/ Jordi Girona 1-3, 08034 Barcelona, Spain
E-mail: lluis.marsal@urv.cat Phone: +34 977 559 625, Fax: +34 977 559 605

Abstract

Ordered macroporous silicon and self-ordered nanoporous alumina were used as templates to fabricate polymer micro- and nanostructures. Herein we focus on a infiltration method of a Poly(methyl methacrylate) (PMMA) solution into the pores of the template. PMMA pillars with pore diameters from 60 nm to 3 μm and pore depths from 200 nm to 150 μm were obtained.

1. Introduction

In recent years, the fabrication of micro- and nanostructures has been an emerging field of interest due to their potential applications for various kinds of functional devices [1]. Template-assisted technique is one of studied method to fabricate ordered structures. Due to its order, vertically aligned structures, precision and uniformity in a large scale, macroporous silicon is an attractive candidate for use as template in this technique [2-7]. In order to obtain nanostructures, the most common nanotemplate is anodized aluminium oxide [8-11]. Under appropriate anodization conditions, long-range-ordered anodic porous alumina with an ideally ordered hole arrangement can be obtained [12]. These porous structures have a wide range of applications in the field of functional devices, such as cellular engineering, solar cells, biosensors, photonic crystals and biomolecular separation [13].

In this study, we describe a template-assisted method to fabricate polymeric micro- and nanostructures. This method entails infiltration of a Poly(methyl methacrylate) (PMMA) solution into the pores of the templates, macroporous silicon and self-ordered nanoporous alumina.

2. Experimental and results

Macroporous silicon templates were prepared by light-assisted electrochemical etching [14]. Silicon substrate open only at one end with a pore depth between 22 μm and 7.5 μm and pore diameter of 2 μm were fabricated. Free-standing silicon membranes with 150 μm of pore depth and pore diameter of 3 μm were obtained as well.

Self-ordered nanoporous alumina was fabricated by using a two step-anodization process in 0.3 M oxalic acid at 15 ºC [15]. Self-ordered nanoporous alumina templates have pore depths between 200 nm and 1.3 μm and pore diameters about 60 nm.

Macroporous silicon and self-ordered nanoporous alumina templates were infiltrate of a PMMA (Poly(methyl methacrylate), Mw = 120,000 purchased from Sigma-Aldrich) solution in toluene. The infiltration was carried out by putting a drop of the solution on top of the sample at room temperature. The samples were heated in order to evaporate the solvent.

Silicon templates were removed by immersing the samples into 40 wt% KOH (aq) at 40ºC. PMMA nanostructures were obtained by the selective dissolution of self-ordered nanoporous alumina in a 1M NaOH aqueous solution for 20 min.

All the samples were inspected using an environmental scanning electron microscopy (ESEM, FEI Quanta 600) operated at low vacuum. In the case of PMMA nanopillars, a thin gold layer was deposited on the samples in order to avoid deformations upon heating during SEM observation.

Figure 1 shows the results of using macroporous silicon as template. PMMA micropillars have diameters ranging from 3 to 2 μm and heights raging from 150 μm to 5 μm. Figure 2 shows PMMA nanopillars with diameters of 60 nm and heights raging from 1.3 mm to 200 nm fabricated using self-ordered nanoporous alumina template. Free-standing PMMA micropillars were produced by using macroporous silicon templates with a pore depth less than 10 μm. PMMA micropillars start to congregate into disordered domains if the pore depth value is higher than 15 μm. Similar results were obtained for PMMA nanopillars obtained from nanoporous alumina with higher pore depth than 300 nm.

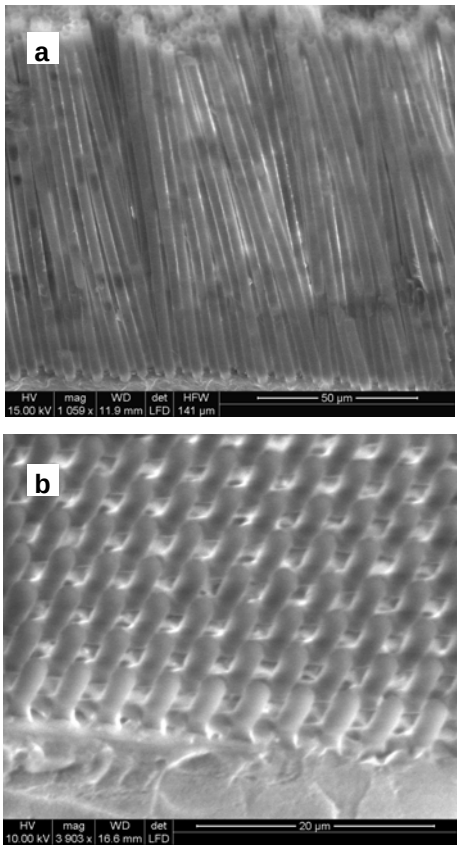

Fig.1. ESEM images of PMMA micropillars after remove macroporous silicon template.

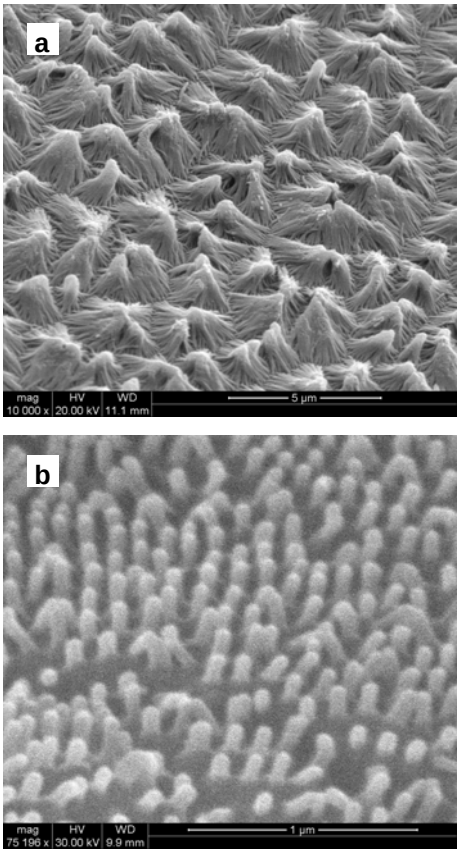

Fig.2. ESEM images of PMMA nanopillars after remove self-ordered nanoporous alumina template.

Acknowledgements

This work was supported by Spanish Ministry of Education and Science (MEC) under grant number TEC2006-06531 and HOPE CSD2007-00007 (Consolider-Ingenio 2010). Josep Ferré-Borrull acknowledges the Ramón y Cajal fellowship from the Spanish Ministry of Science and Technology.

References

[1] a) M. Steinhart, J. H. Wendorff, A. Greiner, R. B. Wehrspohn, K. Nielsch, J. Schilling, J. Choi, U. Gösele, Science **296**, 1997 (2002); b) S. Grimm, K. Schwirn, P. Göring, H. Knoll, P. T. Miclea, A. Greiner, J. H. Wendorff, R. B. Wehrspohn, U. Gösele, M. Steinhart, Small **3**, 993 (2007).

[2] W. Lee, M.-K. Jin, W.-C. Yoo, J.-K. Lee, Langmuir **20**, 7665 (2004).

[3] C.-W. Kuo, J.-Y. Shiu, P. Chen, Chem. Mater. **15**, 2917 (2003).

[4] S. B. Lee, R. Koepsel, D. B. Stolz, H. E. Warriner, A. J. Russell, J. Am. Chem.

[5] P. Jiang, J. F. Bertone, V. L. Colvin, Science **291**, 453 (2001).

[6] S. A. Johnson, D. Khushalani, N. Coombs, T. E. Mallouk, G. A. Ozin, J. Mater. Chem. **8**, 13 (1998).

[7] Y. Y. Li, F. Cunin, J. R. Link, T. Gao, R. E. Betts, S. H. Reiver, V. Chin, S. N. Bhatia, M. J. Sailor, Science **299**, 2045 (2003).

[8] M. Steinhart, R. B. Wehrspoln, U. Gösele, J. H. Wendorff, Angew. Chem. Int. Ed. **43**, 1334 (2004).

[9] M. Zhang, P. Dobriyal, J. Chen and T.P. Russell, Nano Lett., **6**, 5, 1075 (2006).

[10] K. Biswas, Y. Qin, M DaSilva, R. Reifenberger, T. Sands, Phys. Stat. Sol. (a) **204**, 3152 (2007).

[11] T. Yanagishita, K. Yasui, T. Kondo, Y. Kawamoto, K. Nishio, H. Masuda, Chemistry Letters **36**, 530 (2007).

[12] H. Masuda, K. Fukuda, Science **268**, 1466 (1995).

[13] a) D. C. Olson, J. Piris, R.T. Collins, S.E. Shaheen and D.S. Ginley, Thin Solid Films **496**, 26 (2006); b) M. Baba, T. Sano, N. Iguchi, K. Iida, T. Sakamoto and H. Kawaura, Applied Physics Letters **83**, 7, 1468 (2003).

[14] L.F. Marsal, L. Vojkuvka, J. Ferré-Borrull, T. Trifonov, and J. Pallarès, phys. stat. sol. (c), **4**, 1918 (2007).

[15] T. Trifonov, L. F. Marsal, A. Rodríguez, J. Pallarés, R. Al-cublilla, Physica Status Solidi (c) **2**, 3104 (2005).

Numerical simulation of angular-dependent reflectance spectroscopy applied to ordered porous alumina

Z. Král*, J. Ferré-Borrull, L. F. Marsal, J. Pallarès

Nephos, Universitat Rovira i Virgili, Campus Sescelades, Avda. Paisos Catalans 26, 43007 Tarragona, Spain.

*E-mail: zdenek.kral@urv.cat, Phone: +34 977 55 86 53, Fax: +34 977 55 96 05

Abstract

We report a theoretical study of the characterization of ordered porous alumina photonic structures by means of angular-dependent reflectivity. The model is based on the numerical simulation of the interaction of the incident light with the alumina sample. This simulation method allows evaluating the coupling efficiency of the incident plane wave to the photonic modes and the reflection-transmission coefficients. The simulation results show the incident light coupling to different photonic modes that propagate inside the structure at different angles with respect to the surface and demonstrate that with increasing thickness of the sample the number of the modes also increases.

1. Introduction

The characterization of photonic band gap materials is a fundamental issue in the development of the technologies for their fabrication and future application. Several methods for the characterization of photonic band gap materials have been proposed [1, 2]. One of the most widespread techniques is the angular-dependent reflectance spectroscopy (ADRS) [3]. This technique, which is based on the identification of resonant features in the reflectivity spectra at different angles of incidence, has been successfully applied to the characterization of macroporous silicon [4, 5].

In this work we study the possibility of using ADRS to characterize 2D photonic crystals based on self-ordered porous alumina. Porous alumina has attracted a raising interest as a material useful in nanotechnologies thanks to its well-known fabrication process that permits the creation of self-ordered nanometer-sized structures. The study consists of the numerical simulation of the interaction of the incident light with the porous alumina in ADRS measurements. In section 3 we introduce briefly the simulation method and in section 4 we show the preliminary simulations for porous alumina structures with the same characteristics as those obtained in the laboratory [6].

2. Simulation Method

In order to simulate the interaction of the incident light in an angular-dependent reflectance spectroscopy experiment we have used a numerical algorithm based on the scattering matrix treatment proposed by Whittaker *et al.* [7]. This method follows the same approach as the plane-wave expansion (PWE) method but including additional features to calculate the angular-dependent reflectance spectra. The scattering matrix method is based in the fact that the waves propagating inside the structure can be expanded in a sum of plane waves. For instance, for the magnetic field component this expansion can be expressed as:

$$\mathbf{H}(\mathbf{r}, z) = \sum_{\mathbf{G}} \mathbf{h}_{\mathbf{k}}(\mathbf{G}) e^{i\omega t + i(\mathbf{k}+\mathbf{G})\cdot\mathbf{r} + iqz} \qquad (1)$$

This expansion spans over all the vectors ***G*** of the reciprocal space, ***k*** is the Bloch wavevector (since the waves propagating inside the ordered structure must fulfill the Bloch theorem), ***r*** is the position in the x-y plane while *z* is the potion along the scatterers and *q* is the wavevector along the *z* direction. The introduction of the *z* component of the wavevector (*q*) is necessary in order to allow the modeling of waves that propagate inside the photonic crystal in an oblique direction and that can couple to the photonic crystal from the incident medium at a given angle.

By limiting the expansion of eq. (1) to a finite number of reciprocal wavevectors ***G*** and applying Maxwell's equations an eigenvalue problem is obtained *q*, for a given ***k*** and wave frequency ω. The solutions of this eigenvalue problem are the states allowed to propagate inside the sample. Once these states are determined, it is possible to calculate the coupling efficiency of the incident light with a scattering matrix procedure and to obtain the reflection coefficients for the two incident polarizations.

3. Simulation Results

The anodization process to obtain the porous alumina produces pores naturally ordered in a triangular lattice. Consequently, we simulated ADRS for samples consisting of a triangular lattice of circular holes in an alumina transparent host with refractive index n= 1.67. We set the lattice constant (a=153nm) and the size

(r=47nm) of the pores to the average values obtained from actually fabricated self ordered porous alumina samples [6]. Figure 1 shows a SEM picture of an actual sample together with the relevant sizes and measurement directions. Figure 2 shows the photonic band structures for the TE modes. The wavelength scale at the left y-axis shows that some of the photonic bands and band gaps lie in the UV-visible region of the electromagnetic spectrum. Figure 3 shows simulated ADRS for alumina membranes of thicknesses 300nm, 600nm and 900nm (from up to down). The measurements are performed for incident and reflected beams along the ΓM direction and for TE polarization. The picture shows the reflection coefficient versus the frequency of the incident light and its angle of incidence. The 2nd, 3rd and 4th TE bands for this structure (Fig.2) are also shown. It can be seen that for the second TE band there are several resonant features in the ADRS. Such features are related to coupling of the incident light to the photonic modes that propagates inside the structure at different angles with respect to the surface. These photonic modes correspond to different qs that are eigenvalues of the wave equation inside the structure. It is important to remark that the resonant features do not match exactly with the corresponding photonic bands. This is because the photonic bands are calculated for q=0. It can also be observed that with increasing thickness the number of resonant features for a given band also increases.

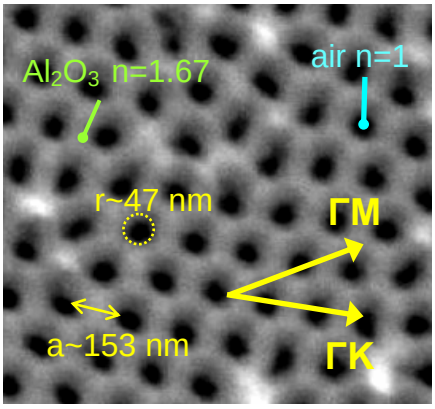

Fig.1 SEM picture of a porous alumina structure where the relevant parameters are indicated.

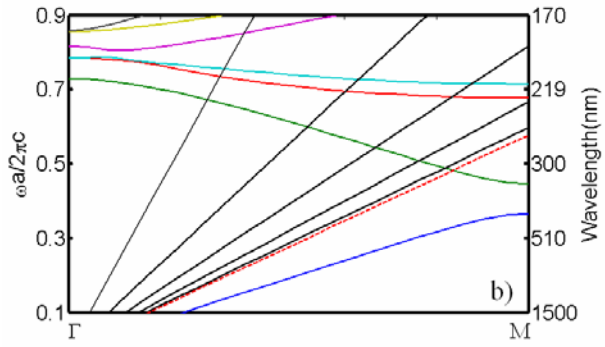

Fig.2 TE bands of the ideal porous alumina considered as 2D photonic crystal.

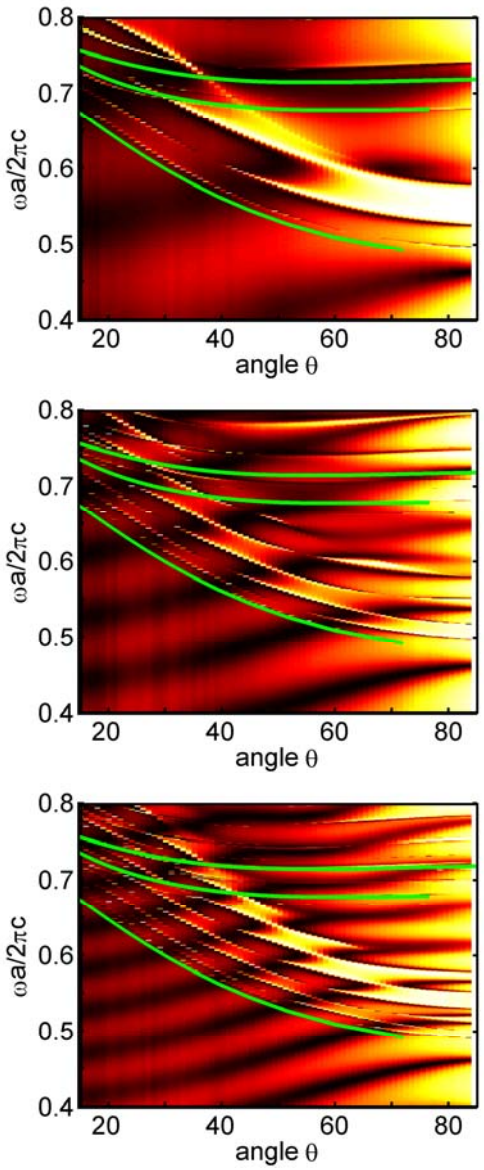

Fig.3 ADRS simulated measurements for porous alumina membranes with thicknesses 300nm (upper), 600nm (center), 900nm (bottom).

References

[1] E. Yablonovitch, T. J. Gmitter, Phys. Rev. Lett. **63** (1989) 1950-1953.

[2] D. Labilloy, H. Benisty, C. Weisbuch, T. F. Krauss, R. M. DeLaRue, V. Bardinal, R. Houdre, U. Oesterle, D. Cassagne, C. Jouanin, Phys. Rev. Lett. **79** (1997) 4147-4150.

[3] V. N. Astratov, M. S. Skolnick, S. Brand, T. F. Krauss, O. Z. Karimov, R. M. Stevenson, D. M. Whittaker, I. Culshaw, R. M. De la Rue, IEE P-Optoelectron. **145** (1998) 398-402.

[4] Z. Král, J. Ferré-Borrull, J. Pallarès, T. Trifonov, A. Rodriguez, R. Alcubilla and L. F. Marsal, Materials Science and Engineering: B, **147**, Issues 2-3, (2008), 179-182

[5] Z. Král, J. Ferré-Borrull, et al., Thin Solid Films, In Press.

[6] L. Vojkuvka, L.F. Marsal, J. Ferré-Borrull, P. Formentin and J. Pallarés, Superlattices and Microstructures, In Press, Corrected Proof, Available online 26 November 2007.

[7] D.M. Wittaker, I.S. Culshaw, Phys. Rev. B, **60**, (1999) 2610-2618.

Porous alumina compatible with micro-machined silicon technology

R. Calavia[a], A. Mozalev[b], V. Khatko[a], E. Llobet[a]

[a] *Dep. Electrònica, Rovira i Virgili University, Tarragona, Spain*
[b] *Department of Micro- and Nanoelectronics, Belarusian State University of Informatics and Radioelectronics, Brovka Str. 6, Minsk 220013, Belarus*

Abstract

In this abstract, different processes to obtain porous alumina on micro-machined gas sensors are presented. A process in order to obtain metal-oxide nanorods as sensing material in gas micro-machined sensor is also presented.

1. Introduction

Metal-oxide gas sensors appear some decades ago. This type of sensors have a lot of applications and are more used every day. The traditional metal-oxide gas sensor had high power consumption because the work temperature is above 400 ºC, but some years ago was developed the micro-machined gas sensor, based in a micro-hot plate. In these sensors the power consumption was reduced up to some miliampers by reducing the area to be heated [1].

The sensitivity of metal-oxide gas sensors is proportional to the area of the sensitive material in contact to the gas [2], so the MEM gas sensors have less sensitivity than the traditional sensors.

In order to increase the sensitivity without increasing the power consumption, it is necessary to increase the area of the active material in contact to the gas without increase the area to be heated. It is possible using two strategies, coating a porous alumina layer by metal-oxide on the heater or use a porous alumina layer as a template to obtain metal-oxide nanorods. In both cases it is necessary to obtain an aluminum anodizing process compatible with the micromachined silicon technology for gas sensors application.

2. Variations in the silicon technology processes

The micro-machined gas sensor to be developed is showed in fig 1. This figure shows the porous alumina layer onto the silicon oxide and the heater. The micro-machined process to obtain this sensor is standard except the anodizing step.

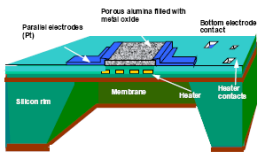

Fig. 1. (b) Micro-machined gas sensor with porous alumina

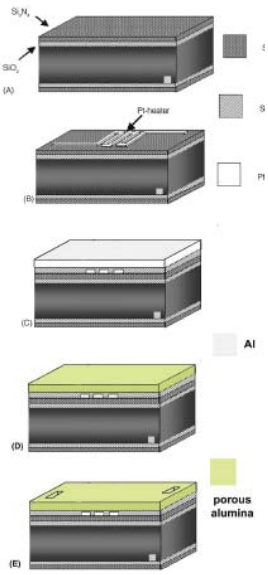

Fig 1 shows that the porous alumina only must be deposited onto the heater, because is the area to be heated. In order to obtain this area properly anodized, it is necessary to anodize the aluminum before the micro-machining process and anodize all the area of the silicon wafer (fig 2). The aluminum layer must be anodized completely, so is necessary to insert a thin (25 – 40 nm) titanium layer, because this material takes a long time to be anodized and allows the aluminum layer to be completely anodized [3].

Fig. 2. (e) Technological steps with anodising before the contact opening

To test the best process in order to obtain porous alumina only on the heating area of the micro-machined gas sensor, three variants were developed in the anodizing processes. The first one is based in the deposition of a photoresist layer. After the exposure and development of the photoresist, the titanium – aluminium bilayer is deposited over the photoresist and the anodizing process can start. When the aluminium layer is completely anodized, the photoresist layer must be removed and the porous alumina only remains in the areas where the photoresist layer was previously removed (typical lift –off process)

The other processes are similar, but the porous alumina must be removed by an etching process. The difference between the processes is based in the step of opening the contacts for the heater, because can be opened before or after (fig 2) the anodizing process.

The wafers that had the contacts opened before anodizing process failed because there was an incompatibility with the standard silicon process. This incompatibility made that the area between the sensors was anodized too fast and the aluminium on the heating area of the sensors was isolated.

The wafers that were anodized before opening contacts

were anodized properly.

3. Variations in the anodizing processes

In order to obtain the highest increase in the sensitivity of the micro-machined gas sensors is necessary to study the influence of the organization, the depth and the diameter of the pores in the porous alumina layer. To make this study was necessary to obtain different thickness of the titanium and aluminium layers for every silicon technology processes studied in this work. The thickness of the titanium layer is similar for all the silicon wafers because his function is centred in the electrical connection of the aluminium layer with the power supply of the electrochemical process.

In the case of aluminium layer, different thickness for every type of processes were tested to allows the test of different anodizing processes. The wafers with a aluminium layer up to 400 nm were anodized by unorganized porous alumina processes (simple anodizing) because their thickness is too low to use self-organized anodizing process [4]. Some wafers were covered with a 800 nm aluminium layer. This thickness leads to two step anodizing process and to obtain self-organized porous alumina [5].

By using different electrolytes in the anodizing electrochemical process leads to control some parameters of the morphology of the pores as, for example, the diameter, since every electrolyte has a typical pore diameter due to that every electrolyte has a typical working voltage [6]. In these wafers were tested two different electrolytes, malonic and tartaric acid [7].

4. Metal-oxide nanorods micro-machined gas sensor

One wafer was destined to test the second strategy to increase the active area in contact to the gas without increasing the area to be heated, the use of metal-oxide nanorods as sensing material. In this case, the sensor has the same structure showed in Fig 1, but the porous alumina is changed by a metal-oxide nanorods layer.

The process to obtain this sensor is similar to the process explained in the anodizing: before opening the contacts for the heater a layer of the metal to obtain his metal-oxide nanorods has to be deposited under the aluminium layer. In the anodizing process, when the aluminium layer is completely anodized, in the end of the alumina pores starts the oxidation of this metal layer and the growth of the nanorods is initialized in this points. When these nanorods have grown, the anodizing process is stopped and the porous alumina layer is removed.

5. Results

In order to test if the wafers were properly anodized, one of the wafers where the contacts were open after the anodization was used to characterize de porous alumina layer. Fig 3 shows a SEM image of this silicon wafer. The thickness of the layers in this wafer is 25 nm for the titanium layer and 400 nm for the aluminium. The electrolyte used in the anodizing process is malonic acid. The diameter of the pores obtained is around 200 nm.

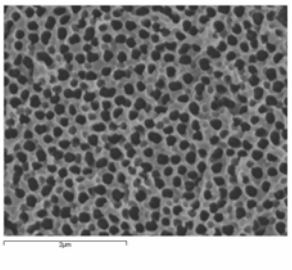

Fig. 3. (d) SEM image of the porous alumina of a wafer with a 400 nm of aluminium layer and using malonic acid as electrolyte

6. Conclusions

The process based in opening the contacts windows before the anodizing process was affected by an incompatibility with the standard silicon technology processes.

The SEM image obtained for one of the wafers indicate that, in the other variants of the processes, the aluminium layer was anodized properly Nevertheless, the final processes are to be developed to obtain the first sensors to be characterised.

References

[1] Mariana Stankova, *Gas sensing properties of rf sputtered WO thin films*, Phd Tesis Universitat Politècnica de Catalunya. 2006.

[2] Marion E. Franke, Tobias J. Kplin and Ulrich Simon, *Metal and metal oxide nanoparticles in chemiresistors: Does the nanoscale matter?*, small 2 No 1, 36-50, 2006

[3] A. R. Walpole, E. P. Briggs, M. Karlsson, E. Palsgard, P. R. Wilshaw, *Nano-porous alumina coatings for improved bone implant interfaces*, Mat. –wiss. U. Werkstofftech. 34, No. 12, 2003

[4] G. E. Thomson, *Porous anodic alumina: fabrication, characterization and applications*, Thin solid films, 297 (1997) 192-201

[5] H. Asoh, K. Nishio, M. Nakao, T. Tamamura and H. Masuda, *Condictions for fabrication of idelally ordered anodic porous alumina using pretextured Al*, Journal of the electrochemical society, 148 (4) B152-B156 (2001)

[6] Sachiko Ono, Noboru Masuko, *Evaluation of pore diameter of anodic porous films formed on aluminium*, Surface and coatings technology, 169-170, 139-142, 2003

[7] V. Khatko, G. Gorokh, A. Mozalev, D. Solovei, E. Llobet, X. Vilanova and X. Correig, *Tungsten trioxide sensing layers on highly ordered nanoporous alumina template*, Sensors and actuators B, 118, 255-262, 2006